

FAR-INFRARED ABSORPTION
IN CUBIC ZnS

By

EDWARD ADAM KWASNIEWSKI, B.SC.

A Thesis

Submitted to the Faculty of Graduate Studies

in Partial Fulfilment of the Requirements

for the Degree

Master of Science

McMaster University

August, 1975

FAR-INFRARED ABSORPTION

IN CUBIC ZnS

MASTER OF SCIENCE
(Physics)

McMASTER UNIVERSITY
Hamilton, Ontario

TITLE: Far-infrared absorption in cubic ZnS

AUTHOR: Edward Adam Kwasniewski, B.Sc. (McMaster University)

SUPERVISOR: Dr. W. R. Datars

NUMBER OF PAGES: viii, 63

SCOPE AND CONTENTS:

Far infrared absorption, in the semiconductor (cubic) ZnS, attributed to single and two-phonon processes was studied under high resolution conditions. Two-phonon absorption was compared with two-phonon density of states curves calculated employing parameters derived from inelastic neutron scattering experiments. Combination phonon modes and their location in the Brillouin zone which give rise to strong features in the two-phonon density of states curves were identified.

ABSTRACT

The shapes, frequencies and intensities of far-infrared absorptions in cubic ZnS, measured by a high-resolution, low-noise far-infrared Fourier transform spectrometer system, and attributable to two-phonon processes, were found to compare favourably with a theoretical two-phonon density of states curve calculated with a program supplied by G. Dolling (1974). The parameters used in the theory were derived from inelastic neutron scattering experiments by Vagelaxós et. al. (1974). Two-phonon combinations and their locations in the Brillouin zone which give rise to strong features in the two-phonon density of states were identified by comparing theory and experiment. Important critical points were discovered on or near the zone boundary and not only at the symmetry points Γ , X, L and W as previously suggested.

ACKNOWLEDGEMENTS

I should like to thank my supervisor, Dr. W. R. Datars for his advice and assistance, especially during the writing of this thesis. Very special thanks go to Dr. E. Koteles for his patience and help during the past two years. Many others have aided me in this work. In particular I should like to thank Dr. G. Dolling for his generosity in providing his two-photon density of states program and Bowmar Canada Ltd. for supplying the cubic ZnS crystal used in these experiments. I should also like to acknowledge the help and friendship of the lab group, especially Mr. F. Holroyd, without whose help the computer would have been my death. Special thanks are given to all my friends in the Solid State group who helped me stay sane before and during the writing of this thesis. I should also like to thank Mrs. H. Kennelly for swiftly and accurately typing this thesis even when she had better things to do. Finally I would like to thank Ms. Lucy Noviks for getting me to finally finish this work by setting the date of our wedding in mid-August.

This research was supported through grants from the National Research Council of Canada. Personal financial support from the Government of the Province of Ontario and McMaster University is gratefully acknowledged.

TABLE OF CONTENTS

<u>CHAPTER</u>		<u>Page</u>
I	INTRODUCTION	1
II	INSTRUMENTATION AND SAMPLE	
	A - Far-infrared Interferometer	
	i - Introduction	4
	ii - Fourier transform spectrometer	5
	iii - Instrument optimization	
	a - Path Difference Errors	6
	b - Intensity Errors	9
	B - Peripheral Equipment	
	i - Sample Assembly	
	a - Description	11
	b - Sample Preparation	14
	c - Detector	14
	ii - Data Acquisition	14
	C - Computation	16
III	LATTICE ABSORPTION - THEORETICAL FITTINGS	
	A - Introduction	18
	B - Fittings	
	i - Dispersion curves for cubic ZnS	24
	ii - Density of states and critical points	28
IV	LATTICE ABSORPTION - EXPERIMENTAL OBSERVATIONS	31
V	LATTICE ABSORPTION - DISCUSSION	
	A - Single-phonon Absorption	37
	B - Two-phonon Absorption	38
VI	CONCLUSIONS	52
	BIBLIOGRAPHY	62

LIST OF FIGURES

<u>Figure No.</u>		<u>Page</u>
2.1	Top view of the optical system of the far-infrared Fourier transform spectrometer	7
2.2	Schematic cross-sectional view of sample assembly	12
2.3	Block schematic diagram of data acquisition system	15
3.1a	The Brillouin zone of cubic ZnS	
3.1b	Discontinuities in the phonon density of states produced by four types of critical points in the Brillouin zone	23
3.2	Phonon dispersion curves for cubic ZnS	25
3.3	Contours of constant energy for the $2\nu_1$ combination in the (1,0,0), (1,1,0) and (1,1,1) planes	29
4.1	Three experimental absorption spectra corresponding to beamsplitter and filter combinations in Table 4.1	33
4.2a	Composite experimental absorption spectrum formed by overlapping of spectra in Figure 4.1	
4.2b	Density of states for sum processes	34
4.3	Experimental difference mode absorption spectrum compared to two-phonon density of states for difference processes	35

Figure No.

Page

- 5.1 Observed absorption compared with the calculated density of states for two-phonon summation processes in the frequency range 120-300 cm^{-1} 40
- 5.2 Observed absorption compared with the calculated density of states for two-phonon summation processes in the frequency region 300-450 cm^{-1} 43
- 5.3 Observed absorption compared with the calculated density of states for two-phonon difference processes in the range 120-260 cm^{-1} 50

LIST OF TABLES

<u>Table No.</u>		<u>Page</u>
3.1	Fitted parameters for cubic ZnS with generating GaP parameters from Yarnell et. al. (1968) and minimized error function values.	27
4.1	Three beamsplitter and filter combinations used to measure spectra shown in Figure 4.1.	32
5.1	Assignment of two-phonon summation processes in the region $120-300\text{ cm}^{-1}$	42
5.2	Assignment of two-phonon summation processes in the region $300-450\text{ cm}^{-1}$	46
5.3	Assignment of two-phonon summation processes in the region $450-550\text{ cm}^{-1}$	48
6.1	Summary of all features on the two-phonon sum and difference absorption spectra in this work.	53
6.2	Algebraic generation of sum modes on the hexagonal face of the Brillouin zone using the $\nu_{4,5}-\nu_1$, $2\nu_2$, $2\nu_3$ and $\nu_3+\nu_{4,5,6}$ modes as starting point	56
6.3	Algebraic generation of sum modes at the X point	58
6.4	Algebraic generation of sum modes at the L point	59
6.5	Comparison of two-phonon assignments of various workers	60

CHAPTER I

INTRODUCTION

The frequencies of the normal modes of lattice vibration give results of significance for many of the properties of solids and assist in the deduction of interatomic force laws for the crystal. Techniques of spectroscopy have been extended during the past 25 years to very low frequencies in the far-infrared and one of the fruits of these developments has been the possibility of studying the vibrational states of crystal lattices by spectroscopic means.

Recent advances in technology which have made the far-infrared region of the spectrum readily accessible to experimentation include the far-infrared interferometer, the Fast Fourier Transform (FFT) algorithm, high-speed and high-capacity computers and high sensitivity detectors. A discussion of the Fourier transform spectrometer employed in these experiments is given in Chapter II along with information about the peripheral equipment.

The lattice vibrations of cubic ZnS have been the subject of a number of investigations in recent years. Deutsch (1962) investigated the infrared absorption in the region from 1 to 24 μ and interpreted the resulting spectrum in terms of two and three phonon combination bands of four average zone boundary

phonons. The interpretation, however, was not unique and other interpretations of Deutsch's data were attempted by Marshall and Mitra (1964) and by Johnson (1965), but ambiguities still remained and information was lacking, particularly in the case of the transverse acoustic mode. Recently Nilsen (1969) investigated in detail the Raman spectrum of ZnS and interpreted the second-order Raman spectrum in terms of two phonon combinations of four average frequencies at the zone boundary. In a more recent article, Irwin (1970) presented an alternate interpretation of the data of Deutsch and Nilsen. This interpretation was carried out using a theoretical model introduced by Banerjee and Varshni (1969) and the results of Feldkamp et.al. (1969). Irwin attempted to analyze the previous spectra in terms of scattering from the four critical points $\Gamma(0,0,0)$, $X(1,0,0)$, $L(0.5,0.5,0.5)$ and $W(1,0.5,0)$.

In this work we present a somewhat different interpretation of the two-phonon absorption in cubic ZnS. The high resolution Fourier transform spectrometer used in these experiments allowed us to measure the far-infrared spectrum of cubic ZnS over a range $100-900 \text{ cm}^{-1}$ with great accuracy. The interpretation was carried out using a theoretical shell model introduced by Dolling (1965) and the inelastic neutron scattering data of Vagelatos et.al. (1974). A discussion of Dolling's model and the fitting made to Vagelatos' data is given in Chapter III, along with an example of the resulting density of states and energy contour plots. The spectra obtained in these experiments are

given in Chapter IV and the identification of all the major features of the two-phonon absorption spectra with combination phonon modes at certain points in the Brillouin zone is outlined in Chapter V. The interpretation is accomplished with the aid of the calculated two-phonon density of states curve obtained employing parameters derived from inelastic neutron scattering experiments.

Chapter VI contains a summary of the results and conclusions.

CHAPTER II -

INSTRUMENTATION AND SAMPLE

A - FAR-INFRARED INTERFEROMETER

i - Introduction

Interferometry has had a long and relatively uneventful history until recently. Loewenstein (1966) has presented an interesting review of the early history of this subject. In simplified terms, interferometry is a method of deducing the electromagnetic spectra of a source by analyzing the interference of two coherent beams from the source. An interferogram, which is in reality a Fourier transform of the spectrum, is the result when the intensities are measured as a function of the difference in optical path between the two beams.

In general, interferometry remained a specialized tool for high resolution work until approximately twenty-five years ago when the two dominant advantages of interferometry over classical spectroscopy were discovered. It was Jacquinot and Dufour (1948) who pointed out that, unlike the case of a dispersive instrument, it is not necessary, in an interferometer, to limit the aperture to work at high resolutions. At some given resolution then, the energy throughput of the interferometer is greater than that of a dispersive monochromator which, in effect, reduces the time required for a spectrum with a given signal-to-noise ratio. A few years later Fellgett (1951) showed the advantages of the

multiplex principle which the interferometer employs. Unlike classical monochromators which record information from each resolution element in a spectral band sequentially, the detector of an interferometer has incident upon it radiation from all spectral elements simultaneously. The multiplex principle is a real advantage only if the noise is detector limited. It is evident then that both the multiplex and throughput advantages have their greatest impact in energy starved regions of the spectrum such as the far-infrared. In addition, absolute wavenumber accuracy is guaranteed by the known wavelength used for carriage control, the physical apparatus is inherently simple, and both stray light and overlapping spectral orders are eliminated. In recent years, the addition of low-noise, high-sensitivity detectors, high-capacity, high-speed computers and Fourier transform algorithms, has resulted in a veritable explosion in the number of studies and uses of interferometers.

ii - Fourier transform spectrometer

The Fourier spectrometer used in these experiments is a commercial instrument, FS-720, built by Research and Industrial Instruments Company of England. It is essentially similar to a Michelson interferometer with the notable difference being the size of the optical components. The mirrors and beamsplitter are three inches in diameter so that they may function more efficiently in the far-infrared region of the spectrum.

A schematic diagram of the optical system is given in Figure 2.1. Energy from the Source, S, a high pressure mercury lamp, is collimated by an off-axis parabolic mirror, M_1 , which directs the radiation to a beamsplitter, B. Ideally, the beamsplitter divides the light into two beams with the same amplitude, sending one beam to a moving mirror, M_M , and the other to a fixed mirror, M_S . The light is reflected from these mirrors and recombines at the beamsplitter where half of the energy returns toward the source and is lost while the other half exits toward the condensing mirrors, M_2 and M_3 and the sample assembly. The recombination is either constructive or destructive, depending upon the wavelength of light and the optical path difference between the two beams. Since the beamsplitter is an unsupported single-layer dielectric film (Mylar) it is completely symmetric and so no compensating plate is required.

iii - Instrument optimization

The noise on an interferogram can be subdivided into two classes that are related to its origin; path difference errors and intensity errors.

a - Path Difference Errors

A tacit assumption is made that the interferogram is sampled at constant path difference increments, i.e. at 0, Δx , $2\Delta x$, ... etc. If this is not the case noise and distortion can be generated on the computed spectrum. Periodic errors in the magnitude of Δx produce "ghosts"; a slow progressive error

FIGURE 2.1: Top view of the optical system of the far-infrared Fourier transform spectrometer. The chopper blade is pictured in a horizontal position.

S - Source

C - Chopper Blade

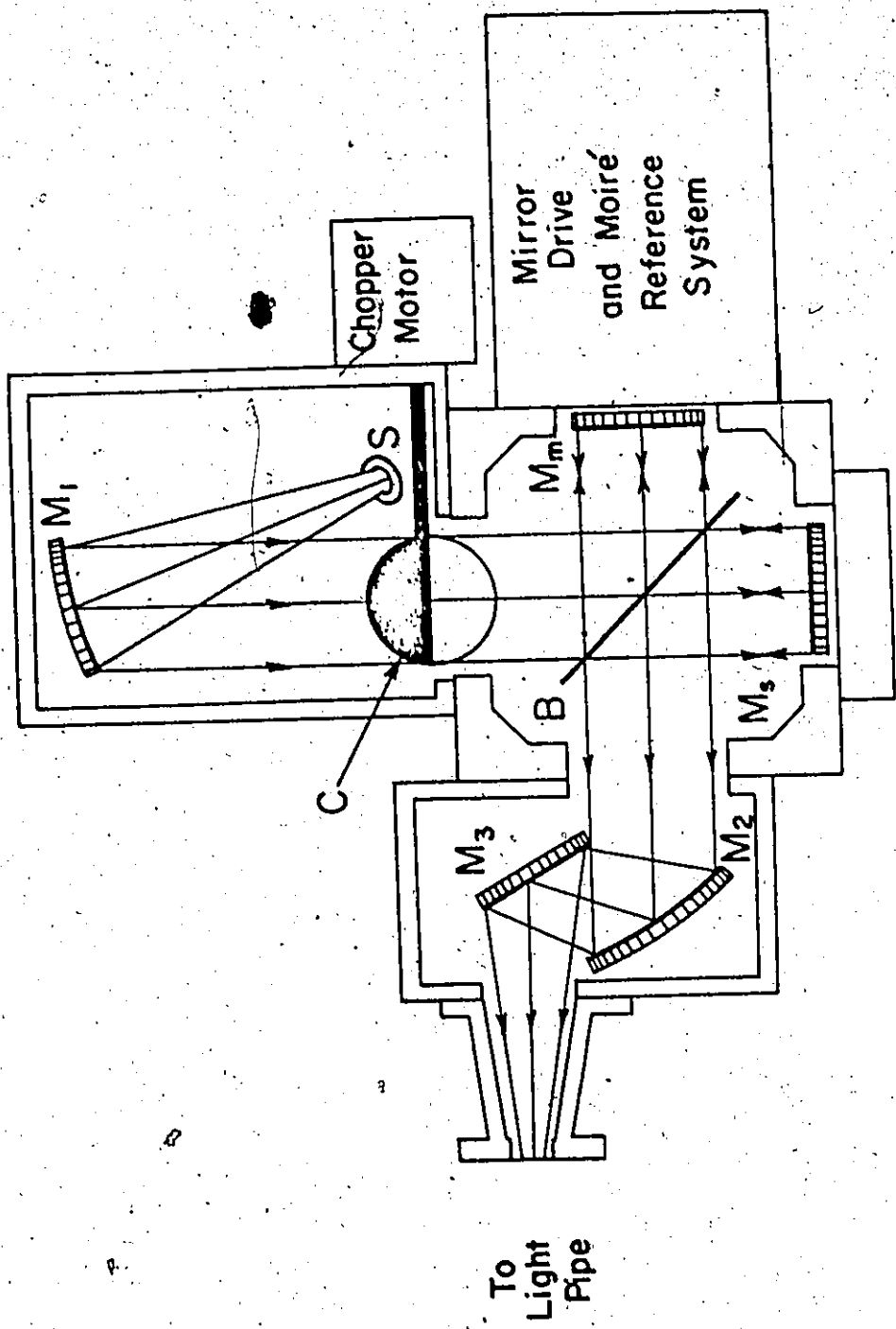
B - Beamsplitter

M₁ - Collimating Mirror

M_M - Moving Mirror

M_S - Stationary Mirror

M₂ and M₃ - Condensing Mirrors



TOP VIEW

reduces the resolving power; a random error produces scattered ripples (Connes and Connes, 1966).

The mirror drive in the present instrument consists of a synchronous motor which is coupled, via a gear box, to a finely machined screw which, in turn, drives a carriage. The gear box permits the velocity of the carriage to be varied from a nominal 0.5 microns per second to 500 microns per second. The moving mirror is mounted on this carriage which advances along a highly precise lapped cylinder. In spite of all these precautions there are indications of jitter and hesitation in the mirror movement. These errors in mirror displacement do not translate directly into errors in path difference as the displacement measuring system is not dependent, to first order, on smooth mirror movement. The reference system consists of two diffraction gratings, one mounted on the carriage and the other fixed to the interferometer base with a spacing of about 25 microns between them. White light from a small incandescent lamp forms Moiré interference fringes as it passes through the gratings and these fringes fall on a photocell. As the carriage moves, the 4 micron ruling of the Moiré gratings produces peaks in the photocell signal spaced 8 microns apart in path difference. This signal is fed through a differential operational amplifier to a Schmidt trigger circuit. The pulse produced every 8 microns is used to command the data acquisition system to read and record an interferogram intensity. Since the maximum sampling interval

is given by $\Delta x = \frac{1}{2} \omega_{\text{max}}$, the upper permissible frequency limit for this sampling system is 625 cm^{-1} (16μ). A system has been incorporated that now allows us to extend our frequency limit to 1250 cm^{-1} (8μ). It takes the signal from the trigger ($\sin \theta$) and doubles the frequency ($\sin(2\theta)$), thus resulting in a pulse every 4 microns to command the data acquisition system. The maximum possible mirror movement is 5 cm (10 cm in path difference) and so the theoretical resolution is 0.1 cm^{-1} .

The absence of "ghosts" in the computed spectrum indicates the absence of systematic errors in the path difference reference system. The effect of random errors is much more difficult to isolate but noise definitely attributable to random path difference errors has not been found.

b - Intensity Errors

Systematic intensity errors such as those introduced by non-linearities in the data acquisition system introduce zero level distortions in the spectrum and harmonic and cross-modulation terms in sharp line spectra. No evidence that this type of distortion is present in this system has been found.

Random intensity fluctuations due to source intensity, detector sensitivity or data acquisition system gain variations add noise to the interferogram and thus the spectrum. The major component of this type of noise in the apparatus has been found to be the light source. The broad band source which emits the greatest intensity in the far-infrared is the high pressure mercury lamp. A 200 watt Gates lamp (UA-2) was used in this in-

investigation. The total far-infrared power incident on the detector was of the order of 10^{-8} watts. A feedback system was set up (Koteles, 1973) so that current was stable to 1 part in 10^5 over one hour. However controlling this did not ensure power stabilization in the lamp since voltage fluctuations were still possible. Furthermore, the total spectral output from the lamp is the sum of contributions from the mercury plasma and the hot lamp envelope (Cano and Mattioli, 1967). Variation in the plasma arc position can generate serious intensity fluctuations of the interferogram. The fringing field from a small (2 kilo-oersteds) permanent magnet was used to lock the arc in a stable position. However this procedure was not always reproducible or reliable. In an effort to reduce the effect of intensity fluctuation from the source, a novel double beam chopping system was devised (Douglas and Timusk, 1974). In this system the signal oscillates between a signal and a lamp reference level unlike ordinary chopping systems where oscillation is between a signal (no blockage) and a zero level (complete blockage of light). The lamp reference is provided by a fixed mirror mounted so that it covers one half of the moving mirror. The chopper then covers first the fixed mirror and then the moving mirror as it rotates and so the detector alternatively receives energy from the moving mirror and the fixed mirror. Uniform intensity fluctuations in the source lead to equivalent changes in the signal and lamp reference levels which then cancel when the signal is rectified and integrated.

The double beam system has the added advantage of eliminating any variations in the signal level that can be correlated with similar variations in the lamp reference level (i.e. changes in detector sensitivity produced by bath temperature changes). The system however has the disadvantage of reducing the throughput by half, and uncorrelated intensity fluctuations such as those produced by mercury arc movement are not cancelled. Using a combination of double beam chopping and magnet stabilization it was usually possible to reduce lamp noise to a level comparable to the detector noise for periods of time longer than an interferogram scan time.

B - PERIPHERAL EQUIPMENT

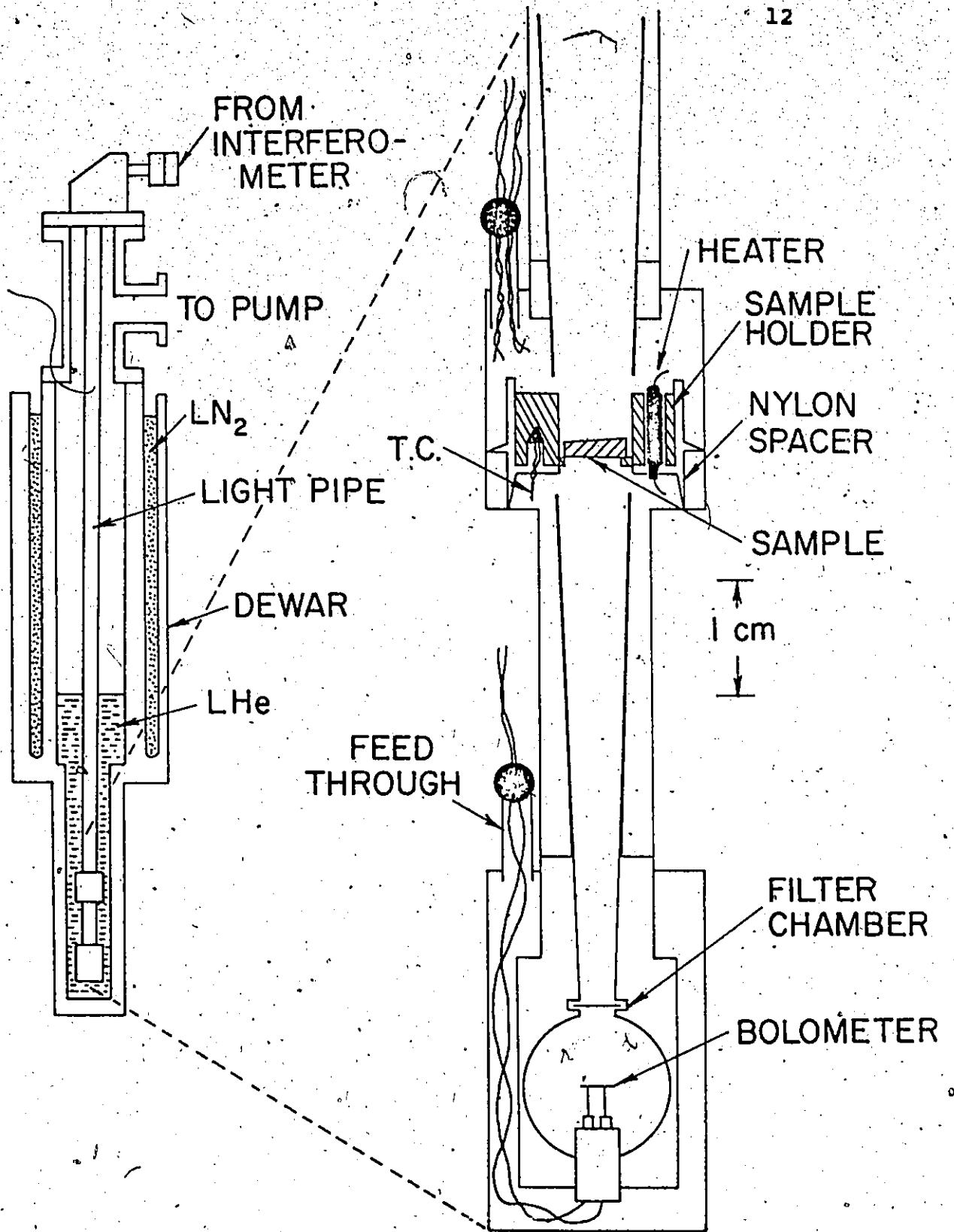
i - Sample Assembly

a - Description

A schematic cross-sectional view of the sample assembly is shown in Figure 2.2. It was designed to permit transmission spectra of a sample to be taken as a function of temperature. The assembly was situated in a stainless-steel Dewar containing the pumped liquid helium bath which kept the detector at its operating temperature of 2°K. Provision was made to increase the temperature of the sample without seriously affecting the operation of the bolometer located 5.5 cm below it.

Light reached the sample chamber after proceeding through about 1 m of 1.3-cm-i.d. polished brass light pipe. A long condensing cone reduced the aperture above the sample chamber.

FIG. 2.2: Schematic cross-sectional view of sample assembly.



The sample holder was a copper cylinder with a 6-mm-diameter hole in the center. The sample was seated, on a lip in this hole, in place, with silver paste. Two holes, 180° apart, were drilled in the sample holder to accommodate a heater, which was a $\frac{1}{8}$ -watt carbon resistor, and a copper-constantan thermocouple (not used). The copper sample holder was thermally insulated from the walls by a nylon spacer. After traversing the sample, the light passed through another condensing cone and a filter chamber before entering a 1.3-cm-diameter integrating sphere which contained the detector.

In order to eliminate the sharp absorption lines in the far-infrared, produced by rotational levels in water molecules, the interferometer and light pipe were kept under a vacuum. The vacuum systems of the interferometer and the sample assembly were separated at the exit of interferometer condensing cone by a filter. Initially, the interferometer was evacuated with a rotary pump which was then valved off and replaced by a sorption pump which eliminated the vibrations inherent in rotary pump operation. The light pipe in the sample assembly was pumped by a rotary and diffusion pump assembly (helium gas was introduced to the light pipe in cold experiments, i.e. sample not heated, to improve coupling between the bath and detector). The elimination of spectral intensity at frequencies greater than ω_{\max} was accomplished by a combination of filters and beamsplitters. A discussion of these is given in Chapter IV.

b - Sample Preparation

The cubic ZnS studied in this experiment was grown by the Eagle Picher Company. The undoped, single crystal obtained was wire cut into the required shape and then lapped with various grades of sandpaper until the proper thickness and wedging was achieved. This resulted in a crystal ranging from 0 to 340 microns in thickness. The surface was not treated in any special way as the absorptions studied in this experiment were due to bulk effects.

c - Detector

The broadband detector employed in these experiments was a gallium-doped germanium bolometer. A very detailed account of the theory of operation of this temperature sensitive resistor has been published by Zwerdling, Smith and Theriault (1968). The bolometer was designed for pumped helium temperatures to benefit from low temperature operation. The temperature attained in the bath was approximately 1.2°K but the static bolometer temperature was twice as large as it was relatively weakly coupled to the bath. The bolometer was constructed following a procedure developed by A. Tumber (1968).

ii - Data acquisition

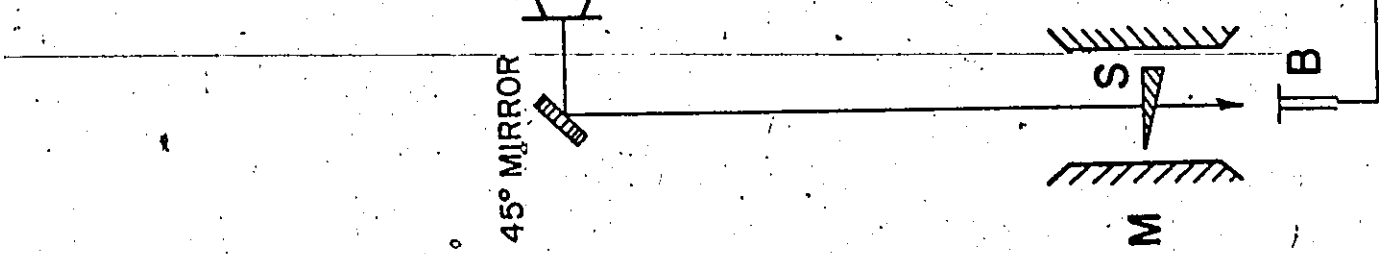
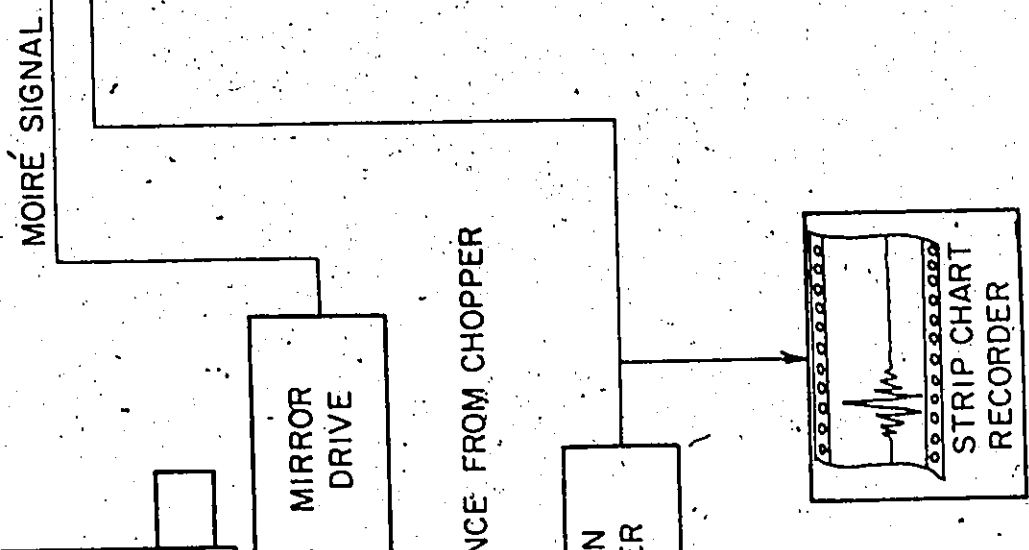
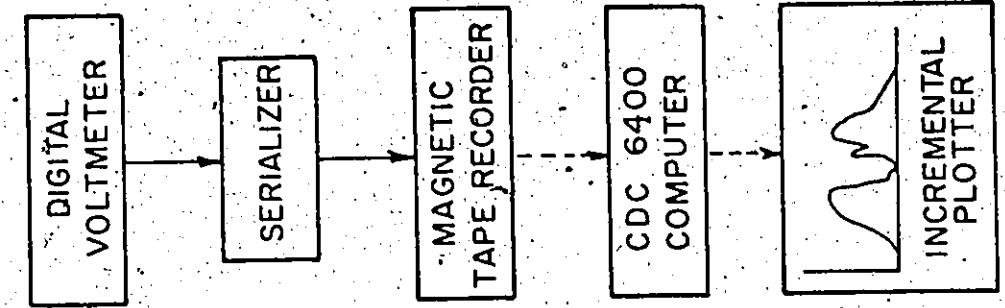
A schematic diagram of the data acquisition system is given in Figure 2.3. The bolometer signal received an initial gain of about 10^8 in the preamplifier (modified version of preamplifier designed by Zwerdling, Theriault and Reichard (1968)). The output of the preamplifier was coupled to the input stage of

Figure 2.3: Block schematic diagram of data acquisition system

M - magnet

S - sample

B - bolometer.



1

2

a laboratory designed and built lock-in amplifier through a 100 to 1 step-up transformer. This amplifier signal was synchronously rectified with the aid of a reference signal obtained from the chopping system. The rectified bolometer signal was integrated by an RC filter (time constant typically 0.1 sec.) and again increased with a D.C. output amplifier. The output of the lock-in amplifier was continuously monitored with a strip chart recorder and digitized by a Hewlett Packard multi-meter (3450 A) capable of resolution of 1 part in 10^5 . The parallel B.C.D. output from the digital voltmeter was sequentially fed into a Digi-Data 1337 incremental tape recorder through a serializer (which also had provision for entering manual records onto the tape). The data in the D.V.M. was written in the magnetic tape whenever a pulse was received from the Moiré reference system.

C - COMPUTATION

The necessity of performing a Fourier transform of the interferogram in order to derive the spectrum has always been the major drawback of interferometry. However, the discovery of the Fast Fourier Transform (Cooley and Tukey, 1965) and the development of fast computers has diminished the problem considerably. Typically in these experiments, 12,500 interferogram points were transformed in about 25 seconds of central processor time on a Control Data 6400 computer.

The computer program was designed first to apodize the interferogram using a triangular function and then to transform

it. The Fourier transform subroutine included a procedure due to Forman et.al. (1966) for correcting zero path difference errors. The computed and corrected spectrum was then either written on magnetic tape for the use of an incremental plotter, presented in the form of a graph by a line plotter or punched on cards for use in averaging and ratioing programs.

CHAPTER III

LATTICE ABSORPTION - THEORETICAL FITTINGS

A - INTRODUCTION

The weak absorptions present in polar materials at frequencies removed from the Reststrahl band (single phonon absorption by transverse optical phonons at Γ) are attributed to multi-phonon processes. They are caused by second order electric dipole moments (Geick, 1965; Borik, 1970), the presence of anharmonic terms in the potential energy associated with lattice vibrations (Cowley and Cowley, 1965; Kleinman, 1960) or a combination of both. Photon-phonon interactions involving three or more phonons are much weaker than those involving two and they can be ignored in the region of the spectrum under study.

Energy and momentum must be conserved in two-phonon interactions. Thus, the sum of the phonon energies and momenta must equal that of the photon,

$$\hbar\omega = \hbar\omega_1 + \hbar\omega_2$$

and

$$\hbar\mathbf{k} = \hbar\mathbf{k}_1 + \hbar\mathbf{k}_2$$

where ω and \mathbf{k} are the frequency and wavevector of the photon and ω_1 , ω_2 and \mathbf{k}_1 and \mathbf{k}_2 the same quantities for the phonons. Since the momentum of a photon is negligible compared with that of typical phonons, only phonon pairs with identical wavevectors may interact simultaneously with the photon. That is $\mathbf{k}_1 = -\mathbf{k}_2$.

In other words, only phonons from equivalent points in the Brillouin zone may interact collectively with the photon. These processes may be additive, resulting in the creation of two phonons or subtractive, resulting in the destruction of one phonon and the creation of another.

In interpreting phonon absorption spectra, the frequency dependence of the coupling mechanism is usually assumed to be so slight and smooth that it can be neglected. Although it is theoretically involved to evaluate precisely the strength of the photon-phonon coupling mechanism for each point in the Brillouin zone, the derivation of selection rules for multiphonon processes at certain symmetry points in the Brillouin zone is relatively straightforward using group theory techniques and coupling mechanism models. The selection rules for two-phonon-photon interactions at certain symmetry points have been derived by Birman (1963) for absorption in the zinc-blende structure. Selection rules are only of limited use however because, although they specify whether or not a particular two-phonon process is permitted they provide no information on the strength of the interaction. Further, they have been calculated only at high symmetry points in the Brillouin zone, whereas this work tends to show that most of the absorptions in cubic ZnS originate from critical points on the hexagonal face.

The total two-phonon absorption intensity is dependent not only upon the strength of the two-phonon-photon interaction, but also upon the two-phonon density of states and the thermal

population of these states. The number, n_i , of phonons of frequency, ω_i , as a function of temperature is given by the Bose-Einstein distribution function,

$$n_i = \left[\exp\left(\frac{\hbar\omega_i}{k_B T}\right) - 1 \right]^{-1}$$

where k_B is Boltzmann's constant. The actual probability of a transition (emission or absorption of a phonon) will contain the squares of two matrix elements, of the form (Ziman, 1972)

$$\langle n_i + 1 | a_i^* | n_i \rangle = (n_i + 1)^{1/2}$$

or

$$\langle n_i - 1 | a_i | n_i \rangle = n_i^{1/2}$$

corresponding to the emission or absorption of a phonon respectively. In the above a_i^* and a_i are appropriate creation and annihilation operators. Therefore the probability of a two-phonon summation process is proportional to $(1+n_1)(1+n_2)$. Correcting this by subtracting the probability of a reverse process, the spontaneous emission of a photon and the annihilation of two phonons, we get the temperature dependence of the net absorption is proportional to $(1+n_1)(1+n_2) - n_1 n_2 = 1+n_1+n_2$. In a similar manner the temperature dependence of the intensity of the difference process can be shown to be $(1+n_1)n_2 - (1+n_2)n_1 = n_2 - n_1$. Thus, the temperature dependence of absorption strengths provides a good method of discriminating between two-phonon sum and difference processes. Summation bands are present at low temperature and their intensities show a small increase with increasing temperature. Difference bands are absent at very low temperature but

are evident at higher temperatures with a strong temperature dependent absorption. Absorption resulting from two-phonon difference processes will be present only at frequencies less than the maximum phonon frequency for the crystal (\sim Reststrahl frequency) while absorption due to two-phonon summation processes can occur at all frequencies up to twice the maximum phonon frequency.

Above we assumed that temperature affected only the intensity of multi-phonon absorption. This is strictly true only if the lattice potential is purely harmonic. Anharmonic terms lead to important properties of crystals. Examples are thermal expansion and temperature dependent phonon frequencies. This second example will be mentioned again later in this chapter.

While the variation in the strength of the two-phonon-photon interaction and the temperature may influence the general level of absorption throughout the spectrum, the structural features on the spectrum are mainly determined by variations of the density of states with frequency. It will be clear, from a set of dispersion curves, that a lattice branch is expected to contribute to the density-of-states curve particularly strongly at any frequency at which its dispersion curve remains flat over an appreciable distance along the wavevector axis.

Then $\frac{d\omega}{dk}$ is zero. A dispersion curve refers only to lattice waves in a single direction. The variation of ω in a particular branch for all directions in \underline{k} -space, is a scalar field, $\omega(\underline{k})$, and the density-of-states curve for a crystal should show characteristic features at frequencies corresponding to those

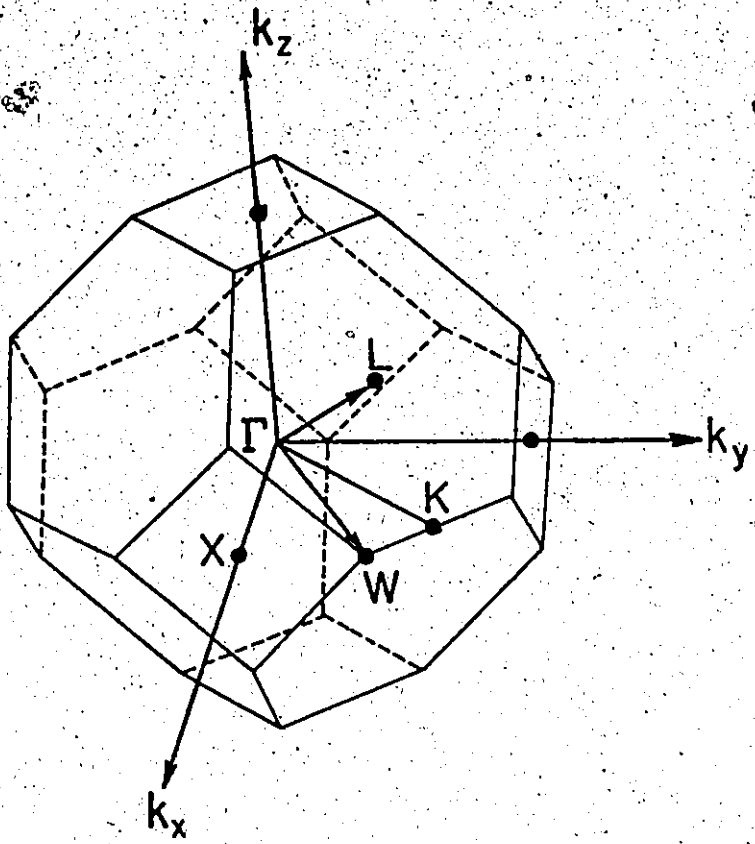
points in \underline{k} -space where $\text{grad } \omega(\underline{k})$ is zero. The importance of infrared absorption of phonon modes is that it makes the accurate determination of the frequencies of the critical points of a crystal practical (and thus the key points in the dispersion curves).

According to theoretical analysis, critical points are to be found at $k=0$ and specific points on the surface of the Brillouin zone in directions of high symmetry. The Brillouin zone of cubic ZnS is a truncated octahedron (Figure 3.1a) and all the phonon branches are predicted to possess critical points at the symmetry positions labelled $\Gamma(0,0,0)$, $X(1,0,0)$, $L(0.5,0.5,0.5)$ and $W(1.0,0.5,0)$. However it will be demonstrated in Chapter V that some of the most prominent features of the phonon spectrum are produced by critical points at positions of lower symmetry at or near the zone boundary or on the hexagonal face.

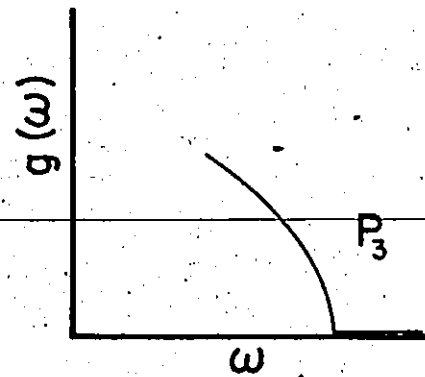
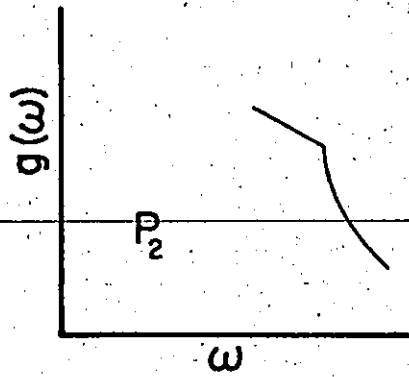
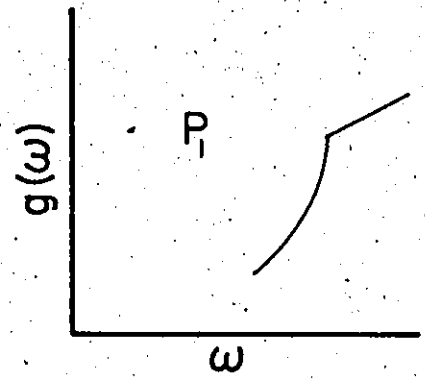
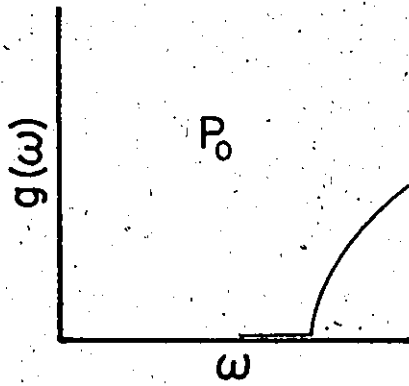
The shape of the discontinuity produced in the density of states by a constant energy volume in \underline{k} space depends vitally on the exact nature of the critical point. Critical points can be of several kinds. $\text{Grad } \omega(\underline{k})$ might equal zero at some \underline{k} because $\omega(\underline{k})$ is a minimum, in three, two, one or no principle directions, i.e. a three dimensional minimum, two kinds of saddle points and a three dimensional maximum respectively. Labeling them P_0 , P_1 , P_2 and P_3 respectively; the associated discontinuities are illustrated in Figure 3.1b. Thus it is possible to correlate critical points in \underline{k} -space not only with frequencies but also with the shapes of the resultant discontinuities in the phonon spectrum. However shape analysis is

Figure 3.1a: The Brillouin zone of cubic ZnS. The Brillouin zone of a F.C.C. lattice is a truncated octahedron. Pictured are the principle directions and the points of high symmetry $\Gamma(0,0,0)$, $X(1.0,0,0)$, $L(0.5,0.5,0.5)$ and $W(1.0,0.5,0)$.

Figure 3.1b: Discontinuities in the phonon density of states produced by four types of critical points in the Brillouin zone: P_0 , a point of minimum phonon energy; P_1 , a saddle point with energy increasing in two principle directions; P_2 , a saddle point with energy increasing in one principle direction; P_3 , a point of maximum phonon energy.



(a)



(b)

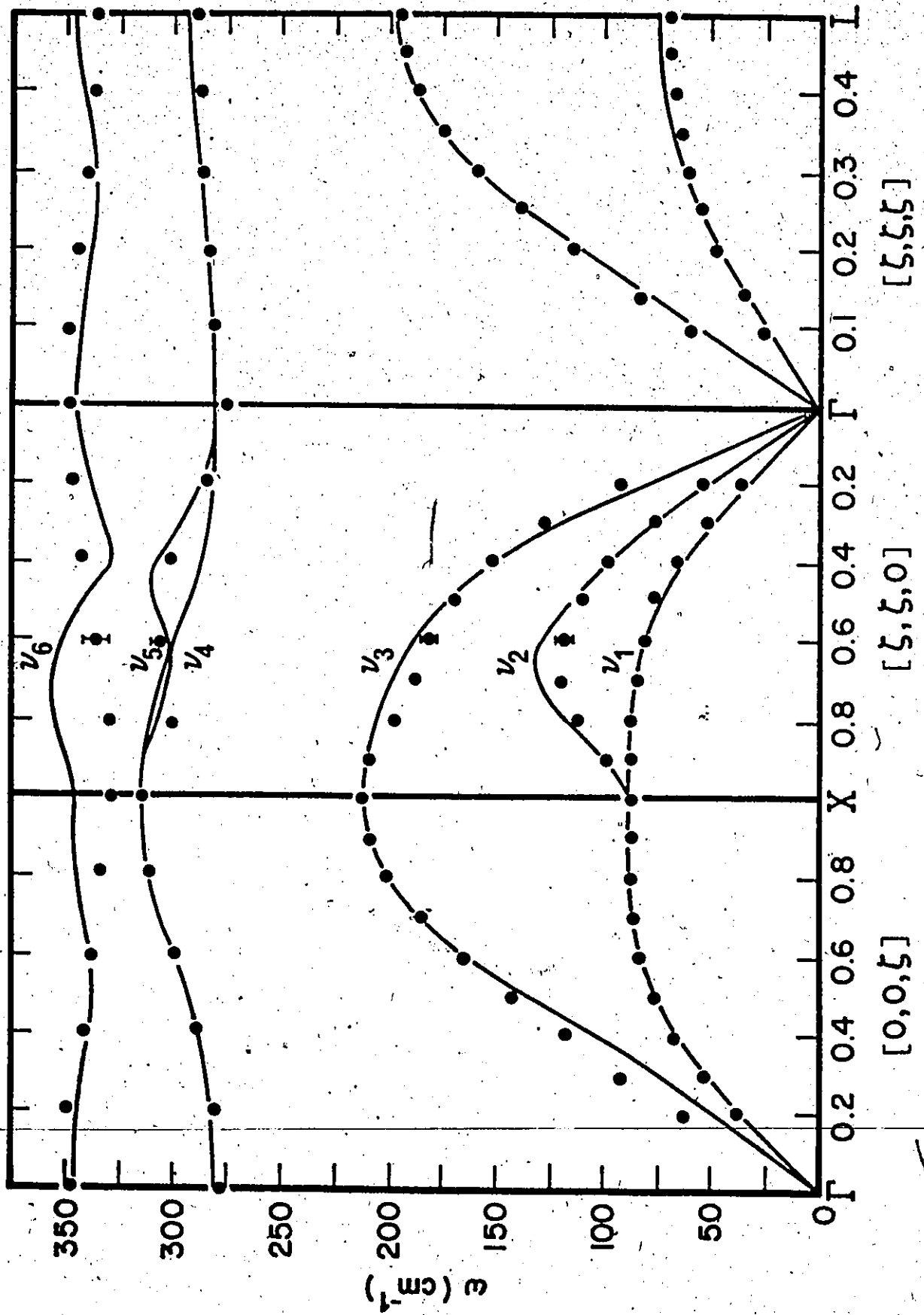
complicated in multiphonon spectra if a great many combination branches are contributing or if two or more branches contribute simultaneously at the same frequency to produce a composite feature. For example, if one branch has a P_1 type discontinuity and another branch a P_2 type discontinuity at the same frequency, a cusp shaped peak will be present in the phonon absorption spectrum. Interpretation of the spectral features may be done more confidently if one has a theoretical fit to experimental dispersion curves. This fit will allow the combination of two or more branches, and with a knowledge of the phonon energies throughout the Brillouin zone, for all branches, the position and shape of important critical points can be discovered using phonon-energy-contour analysis.

B - FITTINGS

i - Dispersion curves for cubic ZnS

Cubic ZnS crystallizes in the zinc-blende structure. This structure is most easily visualized as two face-centered cubic lattices displaced from one another by one-quarter of a body diagonal. For each wave vector there are 3 optical and 3 acoustic normal modes (two atoms per unit cell). The variations of phonon energy with wavevector are recorded in the dispersion curves shown in Figure 3.2. The experimental points were determined by inelastic neutron scattering (Vagelatos et.al. 1974) and the theoretical curves calculated using parameters derived from fitting Dolling's shell model theory (1965) to the neutron experiment.

Figure 3.2: Phonon dispersion curves for cubic ZnS. The circles are the values determined by Vagelatos et.al. (1974) at 300°K by inelastic neutron scattering. The dispersion curves were obtained for phonons propagating in the $[0,0,\zeta]$, $[\zeta,\zeta,0]$ and $[\zeta,\zeta,\zeta]$ directions. Typical error bars are plotted at $(0.6,0.6,0)$. The solid lines are the theoretical dispersion curves calculated using parameters derived from fitting Dolling's shell model (1965) to the neutron data. In the $[\zeta,\zeta,0]$ direction it should be noted that v_5 is always larger than v_4 for all wavevectors (v_4 and v_5 do not cross).



The theoretical dispersion curve of Figure 3.2 represents a least squares fit of Dolling's 14-parameter shell model to the data of Vagelatos et.al. An error function of the form

$$\Delta = \sum_{i=1}^n \sum_{j=1}^6 (\omega_{mij} - \omega_{cij})^2,$$

where ω_{mij} represents the j th measured frequency for the i th wavevector and ω_{cij} represents the j th calculated frequency for the i th wavevector, was used in the program to insure that negative calculated frequencies would produce a positive error. Although the minimizing program could have been started with any set of dummy parameters, the GaP parameters found by Yarnell et.al. (1968) were used in the hope that, because of the similarities of the two compounds, a local minimum could be found sooner. The first thirteen parameters were obtained by fitting the data along the symmetry axes $[0,0,\zeta]$ and $[\zeta,\zeta,\zeta]$ only. The parameter δ was then obtained by keeping the new first thirteen parameters constant and fitting to the data in the $[\zeta,\zeta,0]$ direction. δ has no effect on the frequency values generated in the $[0,0,\zeta]$ and $[\zeta,\zeta,\zeta]$ directions. The best fit parameters are given in Table 3.1, and are compared to the generating GaP parameters. Values of the minimum error are given and can be attributed mostly to the poor fit in the ν_6 branch.

Since it is strictly correct to speak of transverse and longitudinal modes only in certain symmetry directions, the phonons will be labelled ν_1 to ν_6 in order of increasing frequency throughout the zone.

Table 3.1: Fitted parameters for cubic ZnS with generating GaP parameters from Yarnell et.al. (1968) and minimized error function values.

Parameter	GaP	ZnS (cubic)
α_R	32.68 ± 2.4	32.1775
Z_1	0.31 ± 0.12	0.60119
π_1	0.0182 ± 0.0035	0.01819
π_2	0.0119 ± 0.0015	0.0118809
d_1	1.277 ± 0.355	1.31097
d_2	0.990 ± 0.211	1.04192
S_R	1.173 ± 0.177	1.0557
γ_R	0.335 ± 0.064	0.349232
γ_T	0.215 ± 0.055	0.219058
γ_S	0.097 ± 0.049	0.125025
μ	-2.35 ± 0.35	-3.377975
λ	-2.76 ± 0.31	-2.3037875
ν	-0.51 ± 0.21	-1.0880975
δ	2.14 ± 0.25	1.52644

$$\Delta = \sum_{i=1}^n \sum_{j=1}^6 (\omega_{mij} - \omega_{cij})^2$$

$$\Delta(0,0,\zeta) + \Delta(\zeta,\zeta,\zeta) = 2.618$$

$$\Delta(\zeta,\zeta,0) = 3.560$$

$$\Delta_{\text{Total}} = 6.178$$

Note: The parameters for ZnS given above will generate the theoretical dispersion curves and density of states in this work. No proper study has been done to tell us what will be generated if the numbers are rounded off.

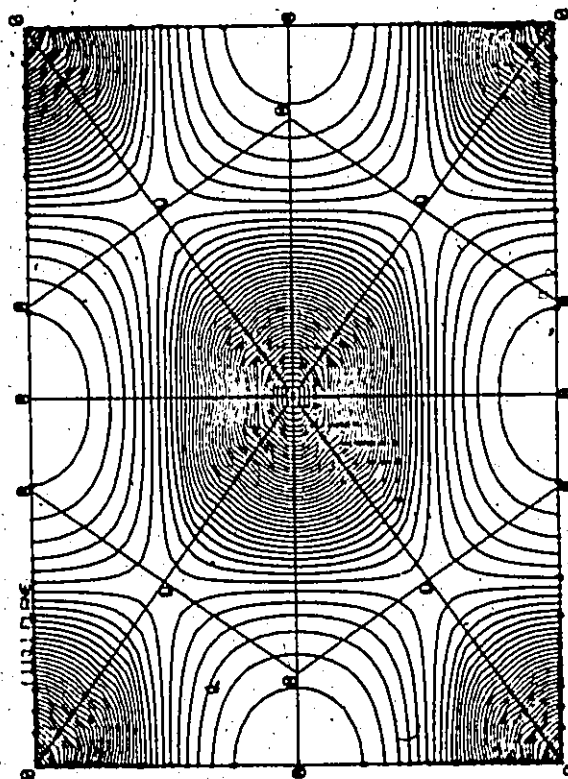
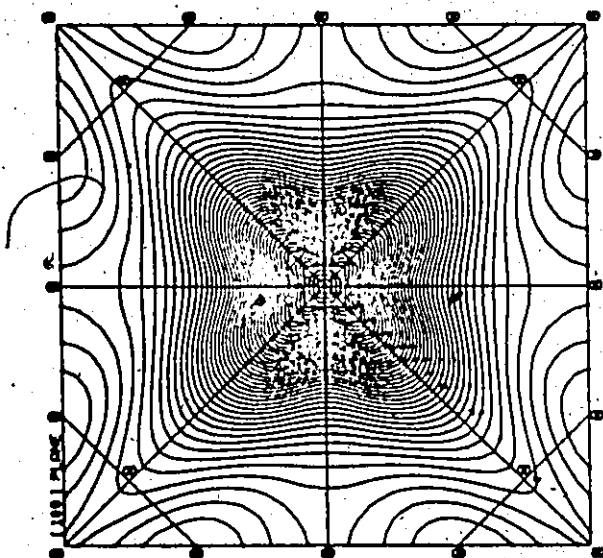
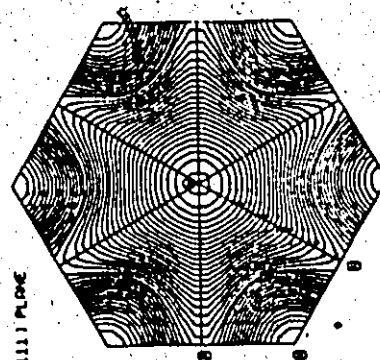
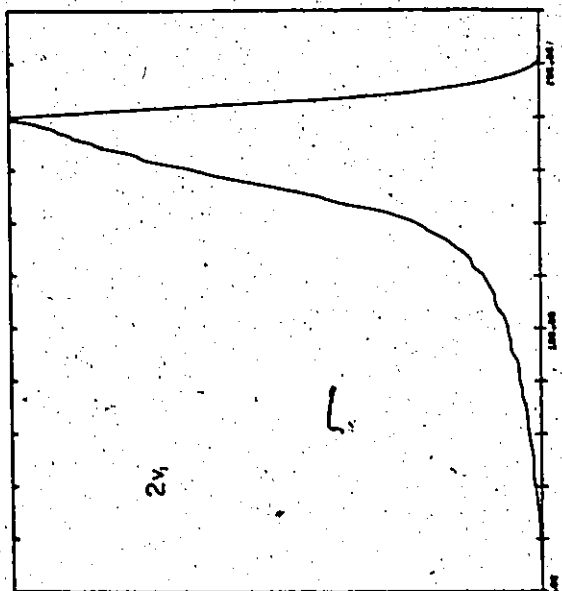
ii - Density of states and critical points

The density of states for the two-phonon modes was calculated by inserting the ZnS parameters from Table 3.1 into a program supplied by G. Dolling (1974). The secular lattice equation was solved at a large number of uniformly distributed points in a forty-eighth of the Brillouin zone (at 874 points) and an interpolation scheme was used to determine extra values for phonon energies between these points. A total of 139,968,000 frequencies for all the phonon branches in the whole zone were obtained using this procedure. To determine the two-phonon density of states curve, two-phonon combination energies were formed by adding or subtracting the frequencies of phonons from different branches but with the same wavevector. The density of states was derived in a straightforward manner by counting the total number of frequencies present in each frequency interval. The second harmonic phonon density (i.e. summing phonons on the same branch) is identical to the single phonon density of states with the frequency scale doubled. No selection rules or frequency dependent coupling mechanisms were applied in these calculations.

These calculations were used to pinpoint the location of critical points in the Brillouin zone. It was assumed that most important critical points were situated on or near symmetry planes. Phonon energies for a particular branch or combination of branches were plotted as a function of wavevector on a specific symmetry plane and contours of constant energy were found and drawn by computer (see Figure 3.3). Critical points were located by searching for areas where the energy was a maximum, a minimum

Figure 3.3:

Contours of constant energy for the $2\nu_1$ combination in the $(1,0,0)$, $(1,1,0)$ and $(1,1,1)$ planes. Also given is the corresponding density of states. All the plots are computer drawn. Critical points are found at Γ (minimum) W (maximum) and L (P_1 type saddle point). A fourth critical point is to be found at X . It is a fluted critical point (Phillips, 1956) and is a P_2 type saddle point. The frequencies are in cm^{-1} . Contours in the $(1,0,0)$ and $(1,1,0)$ planes signify a frequency change of 4 cm^{-1} (starting near Γ at 12 cm^{-1}). Contours in the $(1,1,1)$ plane signify a frequency change of 1 cm^{-1} (starting near L at 154 cm^{-1}).



or exhibited saddle point behaviour. This critical point analysis was used to investigate 21 two-phonon sum modes and 15 two-phonon difference modes on the $(1,0,0)$, $(1,1,0)$ and $(1,1,1)$ planes.

It is evident from a comparison of experimental and theoretical dispersion curves that the overall agreement of the phonon energies in the symmetry directions is good except in the ν_6 branch where, unlike most fittings using Dolling's model, the mode is calculated to curve more than it should. This will result in several ambiguities and errors in both the density of states and contour plots. In order to clarify this situation, the experimental dispersion curves were utilized.

Another point that should be mentioned is that the experimental dispersion curves were measured at room temperature. At low temperature, where the infrared absorption curves were measured, all the phonon frequencies are slightly larger (about 1 to 2%).

CHAPTER IV

LATTICE ABSORPTION - EXPERIMENTAL OBSERVATIONS

The experimental absorption curves obtained covered a range from approximately 100 cm^{-1} to 900 cm^{-1} . Unfortunately no single system of beamsplitter and filters could give an adequately high and constant intensity over the whole range. All possible combinations were found to have areas of low intensity giving low signal to noise. To overcome this problem, three separate beamsplitter and filter combinations were used for the complete region. Each system had a high signal to noise ratio in frequency regions which overlapped sufficiently to allow measurement of the complete spectral region.

Figure 4.1 shows the spectra obtained in the three regions using the beamsplitter and filter combinations given in Table 4.1. The spectra are an average of three or more absorption spectra, taken under identical conditions. Background was eliminated by taking the ratio of the absorption spectra with spectra taken with no sample in the beam. Typically the resolution was 0.4 cm^{-1} . Figure 4.2a shows a composite spectrum obtained by joining the three spectra in Figure 4.1. The corresponding sum mode density of states spectrum is shown

Table 4.1: Three beamsplitter and filter combinations used to measure spectra shown in Figure 4.1

Figure

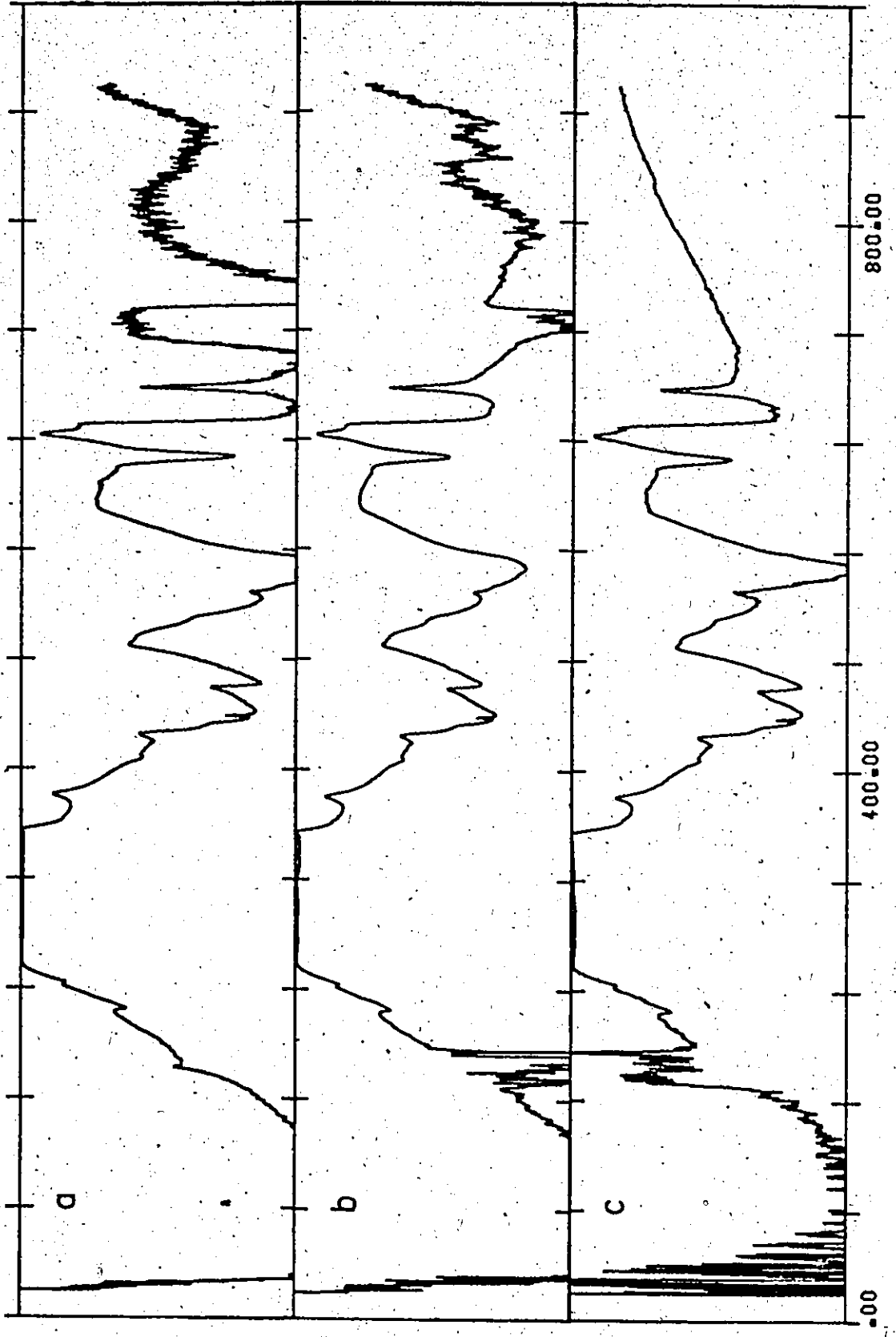
4.1a	B.S.	3.5-4.0 μ mylar
	R.T.	Black polyethylene
	1°K	Black polyethylene
4.1b	B.S.	3.5-4.0 μ mylar
	R.T.	12 μ mylar
	1°K	InSb
4.1c	B.S.	1/8 mil teflon
	R.T.	Polyvinylidene Chloride (Saran Wrap)
	1°K	InSb

note: B.S. - Beamsplitter

R.T. - Filter at top of light pipe

1°K - Filter just before bolometer.

Figures 4.1 a,b,c: Three experimental absorption spectra corresponding to beamsplitter and filter combinations in Table 4.1.



ABSORPTION (ARBITRARY UNITS)

Figure 4.2 a,b: Composite experimental absorption spectrum formed by the overlapping of spectra in Figure 4.1. Comparison is made to density of states for sum processes.

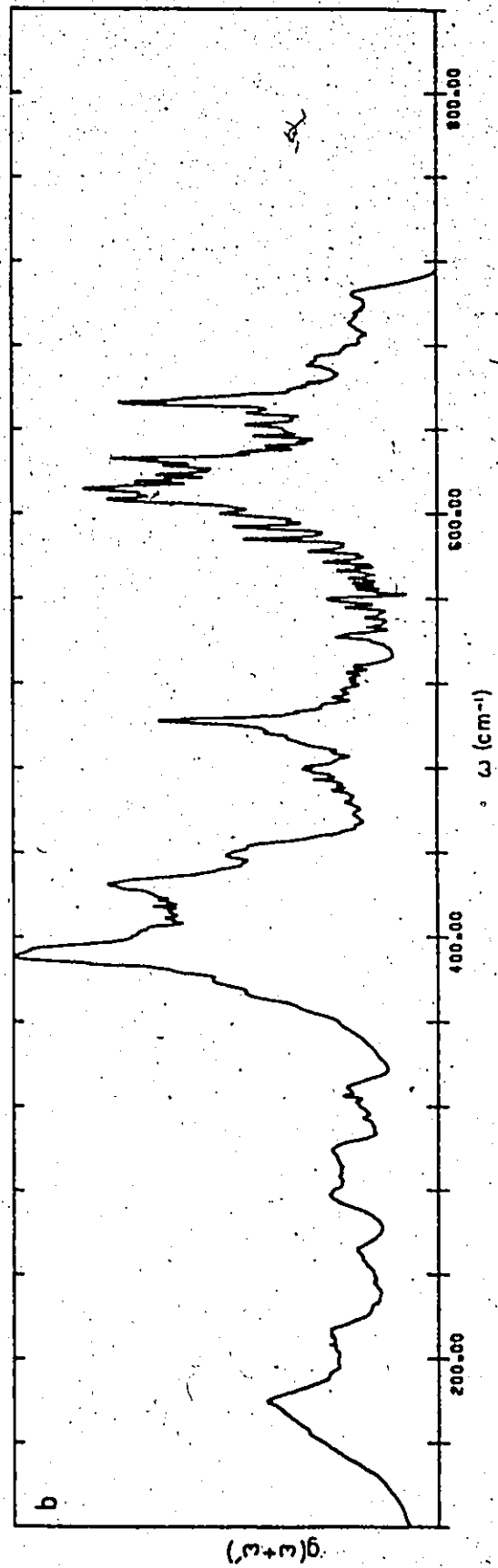
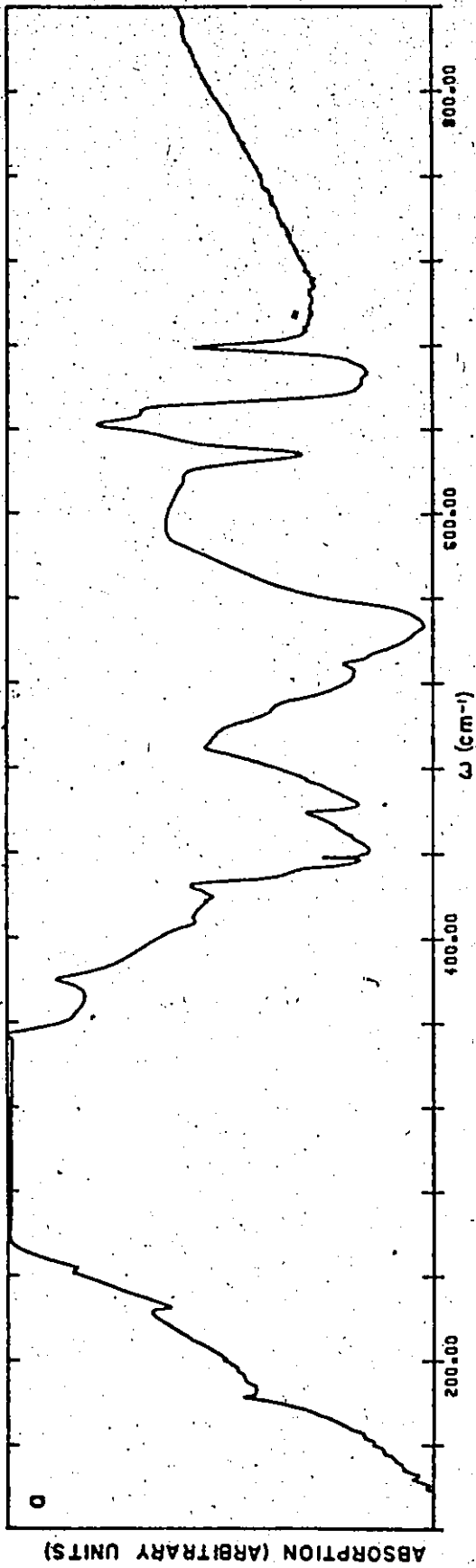
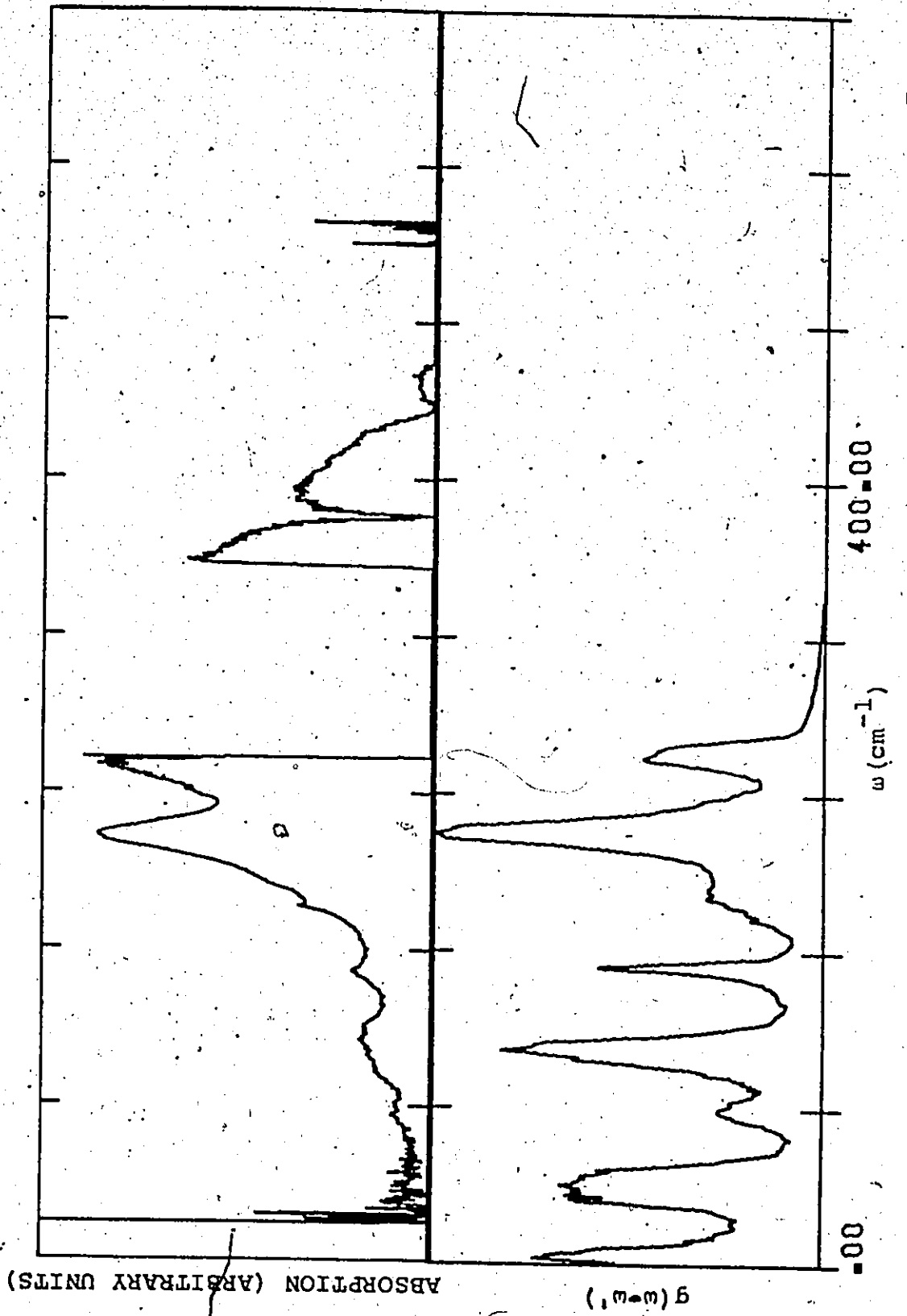


Figure 4.3: Experimental difference mode absorption spectrum
(top) compared to two-phonon density of states
for difference processes.



in Figure 4.2b.

The difference mode absorption spectrum was obtained by heating the sample (heat was obtained by putting current through a resistor situated near the sample) till the interferogram peak intensity was approximately halved. No accurate method for measuring the temperature was available at the time, and it was felt to be unnecessary since no real temperature dependent work was done. Six absorption spectra were averaged in this case because of lower signal caused by increased absorption by the sample and degradation of the bolometer sensitivity because of heat transfer to it. Figure 4.3 shows the experimental difference mode absorption spectrum obtained by ratioing these average spectrum with spectra taken with the sample not heated. A comparison is made to the corresponding density of states spectrum.

CHAPTER V

LATTICE ABSORPTION - DISCUSSION

A - SINGLE-PHONON ABSORPTION

In pure, polar semiconductors, single-phonon absorption is due to first order electric dipole moment induced coupling of the infrared photon to the transverse optical phonon at $k = 0$ (often called Reststrahl absorption). This restriction on the wavevector is necessary in order to conserve momentum as well as energy. In our experiment the broad absorption centered on 304 cm^{-1} (covering the range 250 cm^{-1} to 355 cm^{-1}) is attributed to the Reststrahl absorption.

Early work by Deutsch (1962) and Balkanski et. al. (1964) reported a frequency of 310 or 312 cm^{-1} for the Reststrahl band. This was found to be in disagreement with the value of about 276 cm^{-1} obtained by Raman scattering measurements (and by Bergsma (1970), Feldkamp et.al. (1971) and Vagelatos et. al. (1974) from inelastic neutron scattering). There is, in fact, no evidence of a band around 310 cm^{-1} in the Raman spectrum. Brafman and Mitra (1968) concluded that this band may arise either from an infrared-active two-phonon process or from surface effects.

A possibility then exists that we have two (or more) absorptions smearing together to form the broad absorption centered at 304 cm^{-1} . These two absorptions might possibly be resolved if the sample used could be made thinner, to reduce

the width of the Reststrahl absorption.

B - TWO-PHONON ABSORPTION

The total two-phonon absorption in a crystal is the product of three terms; the strength of the coupling mechanism, the probability of photon-phonon interaction (related to the thermal phonon population) and the two-phonon density of states. The first term will be assumed a slowly and smoothly varying function of frequency in interpreting these absorption spectra. The second can be calculated in a straightforward manner using Bose-Einstein statistics. Most of the features in the absorption can therefore be attributed to discontinuities on the two-phonon density of states.


The agreement between the observed two-phonon absorption and the calculated two-phonon density of states (Figure 4.2) was quite good in the region 120 cm^{-1} to 450 cm^{-1} . However, the agreement was less than adequate in the remainder of the spectra. This is basically due to the very poor fit to the ν_6 branch of the dispersion curve. Questions might also be asked about the fit of the ν_4 and ν_5 branches, especially in the $[\zeta, \zeta, 0]$ direction. Neutron diffraction work in this region is poor, and does not show any splitting as is predicted by the theory (ν_4 and ν_5 branches are degenerate in this region according to experiment). Further complications arise from the fact that the density of states program added noise to the calculated density of states at the high energy end. However, with these problems in mind, some information can still be obtained from the calculated density

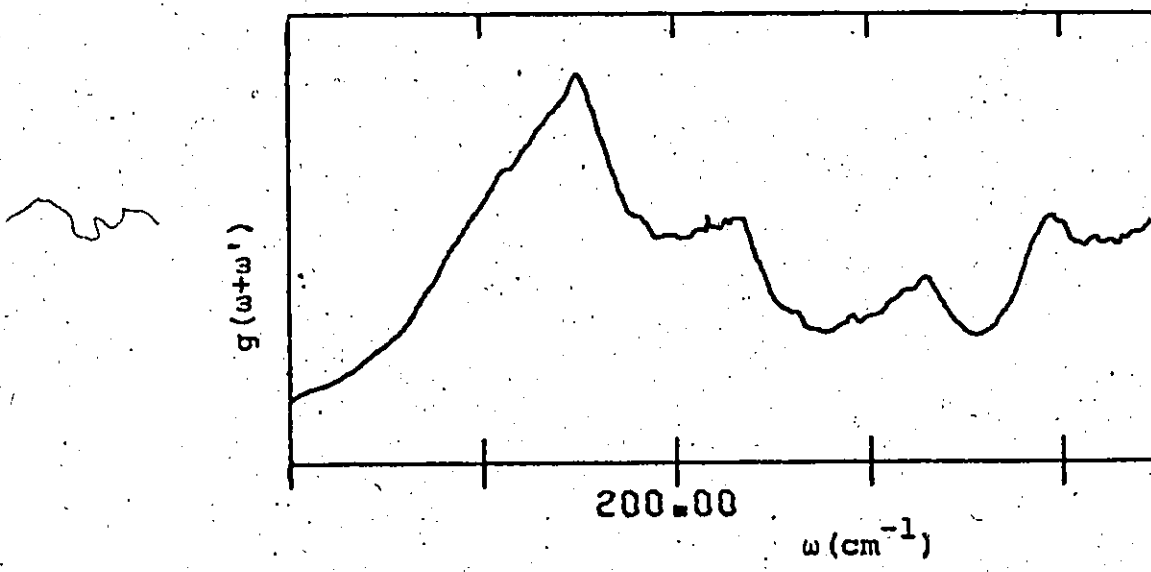
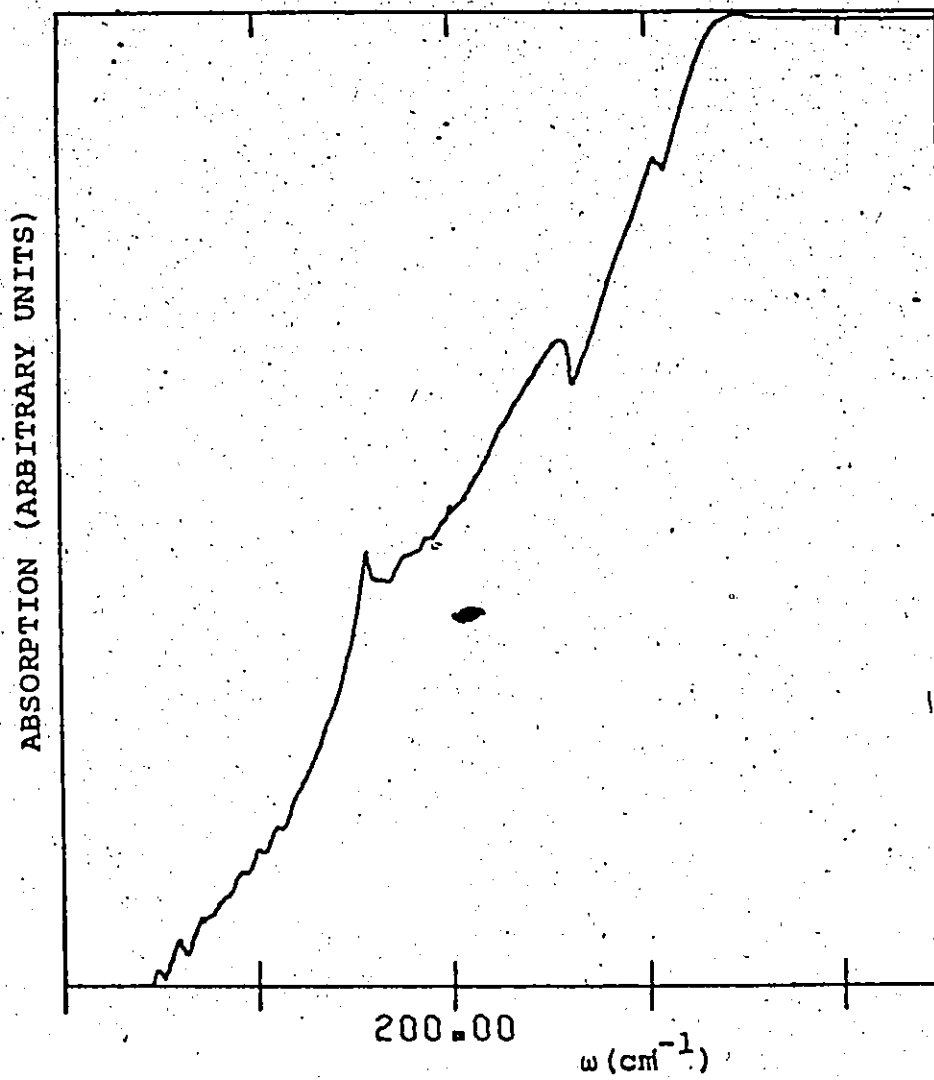
of states. For purposes of discussion, the total absorption spectrum will be divided into four sum regions and one difference region and each will be discussed in detail.

The first sum region consists of features at 183 cm^{-1} , 222 cm^{-1} and 242 cm^{-1} . This region is compared with the calculated density of states for the same region in Figure 5.1. The shapes of the calculated and observed features are similar. However, the frequencies of the observed second and third features are substantially different to the calculated. By comparison with the density of states curve, and by doing a critical point analysis the first peak is attributed to the $2\nu_{1,2}$ modes at X. The critical point analysis indicates that one of the degenerate modes at this point contributes a type P_1 discontinuity ($2\nu_2$) to the phonon density of states and the other a type P_2 . The sum of these produces a fairly weak but sharp peak. The second feature at 222 cm^{-1} is attributed to the $\nu_1 + \nu_2$ mode from the density of states curve. Unfortunately, on looking at the experimental dispersion curves, one will see that even at K the sum frequency is not large enough to account for this absorption. It should be noticed, though, that the calculated dispersion curves at K and L are too large by about $8-9 \text{ cm}^{-1}$. Keeping this in mind and doing a critical point analysis over the hexagonal

7

Figure 5.1: Observed absorption compared with the calculated density of states for two-phonon summation processes in the frequency range 120-300 cm^{-1} . The scale is 40 cm^{-1} per inch.





face we find a type P_3 discontinuity near W at the frequency of the second absorption. The absorption at 242 cm^{-1} is identified with the $2\nu_2$ mode using the density of states curves. It is considered to be a P_2 discontinuity on the hexagonal face along L to K from a critical point analysis and use of the fact that frequencies will be high by about $13\text{-}17 \text{ cm}^{-1}$ at K and L (and probably across the whole hexagonal face too).

It should be noted that although we are quite confident in our identification of the first peak, the critical point identification of the second and third can only be considered tentatively correct. Although the shape of the fitted dispersion curve matches the experimental curve very well there are still areas where the fitting is off by as much as 5%. What this will do to the critical points is unknown.

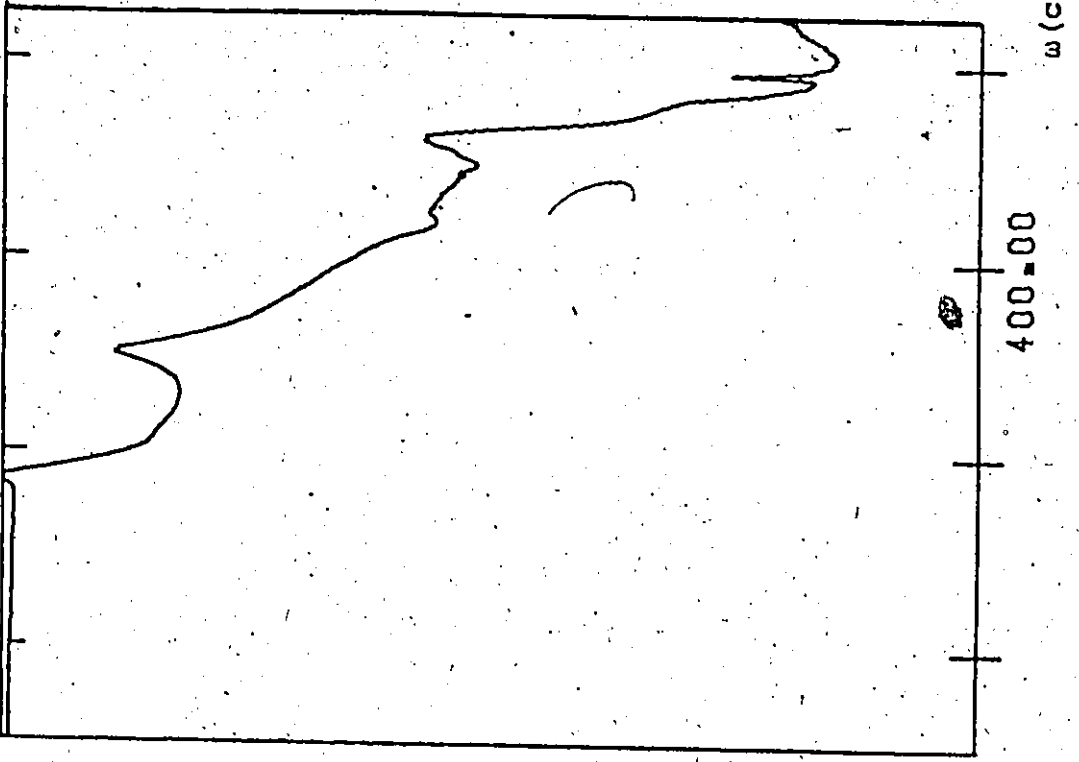
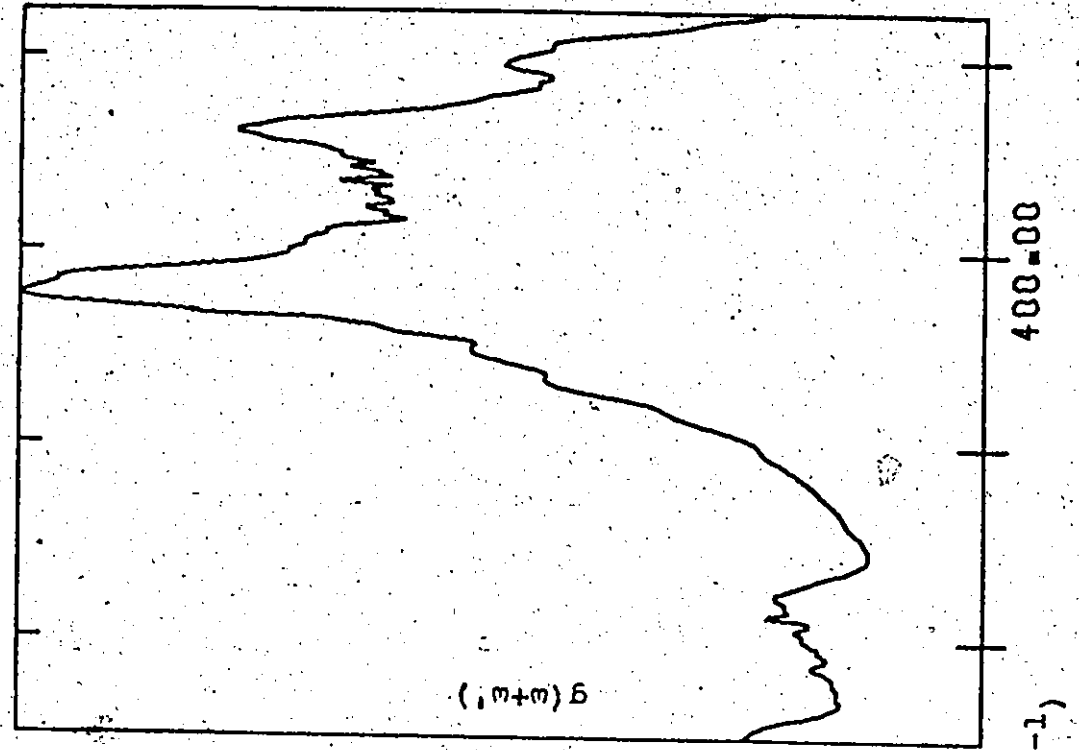
Table 5.1 contains a summary of the features in this region of the spectrum and their assignments.

The second set of absorptions are at 380 cm^{-1} , 424 cm^{-1} and 438 cm^{-1} . They are shown in Figure 5.2 with the calculated density of states for the same region. From the density of states we find that the peak at 380 cm^{-1} is formed by three distinct modes; $2\nu_3$, $\nu_1+\nu_4$ and $\nu_1+\nu_5$. A critical point analysis of $2\nu_3$ reveals degenerate P_1 and P_2 critical points on the hexagonal face of the Brillouin zone. (These critical points are degenerate in energy but not necessarily in momentum (Koteles pg.113, 1973). This will not be mentioned again but should be assumed by the reader for any P_1 and P_2 critical points on the hexagonal face

Table 5:1 Assignment of two-phonon summation processes in the region 120-300 cm^{-1}

Position (cm^{-1})	Combination	Shape	Critical Pt. Location
183	$2\nu_{1,2}$	P_1+P_2	X
222	$\nu_1+\nu_2$	P_3	W
242	$2\nu_2$	P_2	Hexagonal Face

Figure 5.2: Observed absorption compared with the cal-
culated density of states for the two-phonon
summation processes in the frequency region
300-450 cm^{-1} . The scale is 40 cm^{-1} per inch.



ABSORPTION (ARBITRARY UNITS)

4

of the Brillouin zone.) Similar analysis of the $\nu_1 + \nu_{4,5}$ modes shows no comparably strong features, and so it is reasonable to attribute the peak at 380 cm^{-1} to $2\nu_3$. The second large absorption in this second region at 424 cm^{-1} is the most puzzling absorption in the spectrum. There are two peaks between $420\text{--}440 \text{ cm}^{-1}$ in the density of states. The first is attributed to the $\nu_2 + \nu_{4,5}$ modes and the second to the $\nu_1 + \nu_6$ mode. Realizing that our fit in the ν_6 branch of the dispersion curve is poor (and at X and L high from 5-7%) we must look to the experimental dispersion curve to get the proper position of the $\nu_1 + \nu_6$ mode. When we do this we find that $\nu_1 + \nu_6$ is shifted to lower frequencies and in fact to a position close to the $\nu_2 + \nu_{4,5}$ modes. The peak at 424 cm^{-1} is attributed then to the three modes $\nu_2 + \nu_{4,5}$ and $\nu_1 + \nu_6$. A critical point analysis of $\nu_2 + \nu_{4,5}$ shows no strong features that could account for the absorption found. We are left then with $\nu_1 + \nu_6$, only, to attribute to the absorption. As in the case of the $2\nu_3$ mode we believe that this is true and is caused by degenerate P_1 and P_2 critical points on the hexagonal face of the Brillouin zone.

It can be seen from the experimental dispersion curves that the $\nu_{1,2}(X) + \nu_{4,5}(X)$ and the $\nu_{1,2}(X) + \nu_6(X)$ modes are degenerate and have frequencies (corrected to liquid helium temperatures) of approximately 411 cm^{-1} and 432 cm^{-1} respectively. There are two features on the experimental spectrum that correspond to these. A weak peak occurs at 409 cm^{-1} and can be attri-

buted to the $\nu_{1,2} + \nu_{4,5}$ modes at X. Indications are that one of the degenerate sets of modes (most probably $\nu_2 + \nu_{4,5}$) contributes type P_1 discontinuities, while the other type P_3 (or P_2). There is another weak feature at 431 cm^{-1} which is attributed to $\nu_{1,2} + \nu_6$ at X. Critical point analysis suggests possibly a P_1 type discontinuity but this cannot be trusted since the ν_6 fit at X is very poor.

The absorption at 438 cm^{-1} stands out quite differently from the other absorptions in the two-phonon absorption spectrum. It is relatively weak and much sharper than any other feature. It also has no counter-part in the density of states. Experiments by Ibuki et. al. (1968) suggest that absorption due to the localized mode of unassociated Al donors should occur at 437.9 cm^{-1} (at 100°K). We believe this is what is observed in our spectrum.

Table 5.2 contains a summary of the features in the second region of the spectrum and their assignments.

The third sum region of the spectrum includes features at 459 cm^{-1} , 490 cm^{-1} (maximum point) and 529 cm^{-1} . A comparison of absorption curve and the corresponding density of states for this region is not given. At this point in the sum mode density of states noise begins to wash out any information that may be found at a quick glance.

The feature at 459 cm^{-1} is extremely angular, giving the impression of not really being a peak but rather a discontinuity. From the density of states we attribute the absorption to the $\nu_2 + \nu_6$ mode and from a critical point analysis observe a

Table 5.2: Assignment of two-phonon summation processes in the region
300-450 cm^{-1}

Position (cm^{-1})	Combination	Shape	Critical Pt. Location
380	$2\nu_3$	P_1+P_2	Hexagonal Face
	$\nu_1+\nu_{4,5}$	Weak	-
409	$\nu_{1,2}+\nu_{4,5}$	P_1+P_3 (or P_2)	X
424	$\nu_1+\nu_6$	P_1+P_2	Hexagonal Face
	$\nu_2+\nu_{4,5}$	Weak	-
432	$\nu_{1,2}+\nu_6$	$P_1(?)$	X

Note: Localized mode of unassociated Al donors at 438 cm^{-1} .

very strong P_2 type discontinuity near W on the hexagonal face. The feature with a maximum at 490 cm^{-1} is attributed to the $\nu_3 + \nu_{4,5}$ modes. The density of states shows two strong, sharp peaks overlapping to form a single strong, sharp peak. In the experiment the two almost overlap, forming a much broader feature. Critical point analysis suggests degenerate P_1 and P_2 type discontinuities on or just off the hexagonal face for both modes. A smaller feature can be seen on the high energy side of this peak at about 508 cm^{-1} . This feature was always present with the ZnS sample but we have been unable to identify its origin. The feature at 529 cm^{-1} is attributed to the $\nu_3 + \nu_6$ mode. Critical point analysis suggests very strong degenerate P_1 and P_2 type discontinuities on the hexagonal face of the Brillouin zone.

Table 5.3 contains a summary of the features in this region of the spectrum and their assignments.

The final sum mode region is made up of 3 very strong features with maxima at 595 cm^{-1} , 644 cm^{-1} and 678 cm^{-1} . In this region there is very little information to work with because all absorptions are combinations of ν_4 , ν_5 and ν_6 modes which have been poorly fitted to the dispersion curves. However, some information can be found if we realize the limitations of our density of states and contour plots, and draw heavily from the experimental dispersion curves. The feature at 595 cm^{-1} is attributed to the $2\nu_4$, $\nu_4 + \nu_5$ and $2\nu_5$ modes; the absorption at 644 cm^{-1} to the $\nu_{4,5} + \nu_6$ modes; and the feature at 678 cm^{-1} to the

Table 5:3 Assignment of two-phonon summation processes in the region 450-550 cm^{-1}

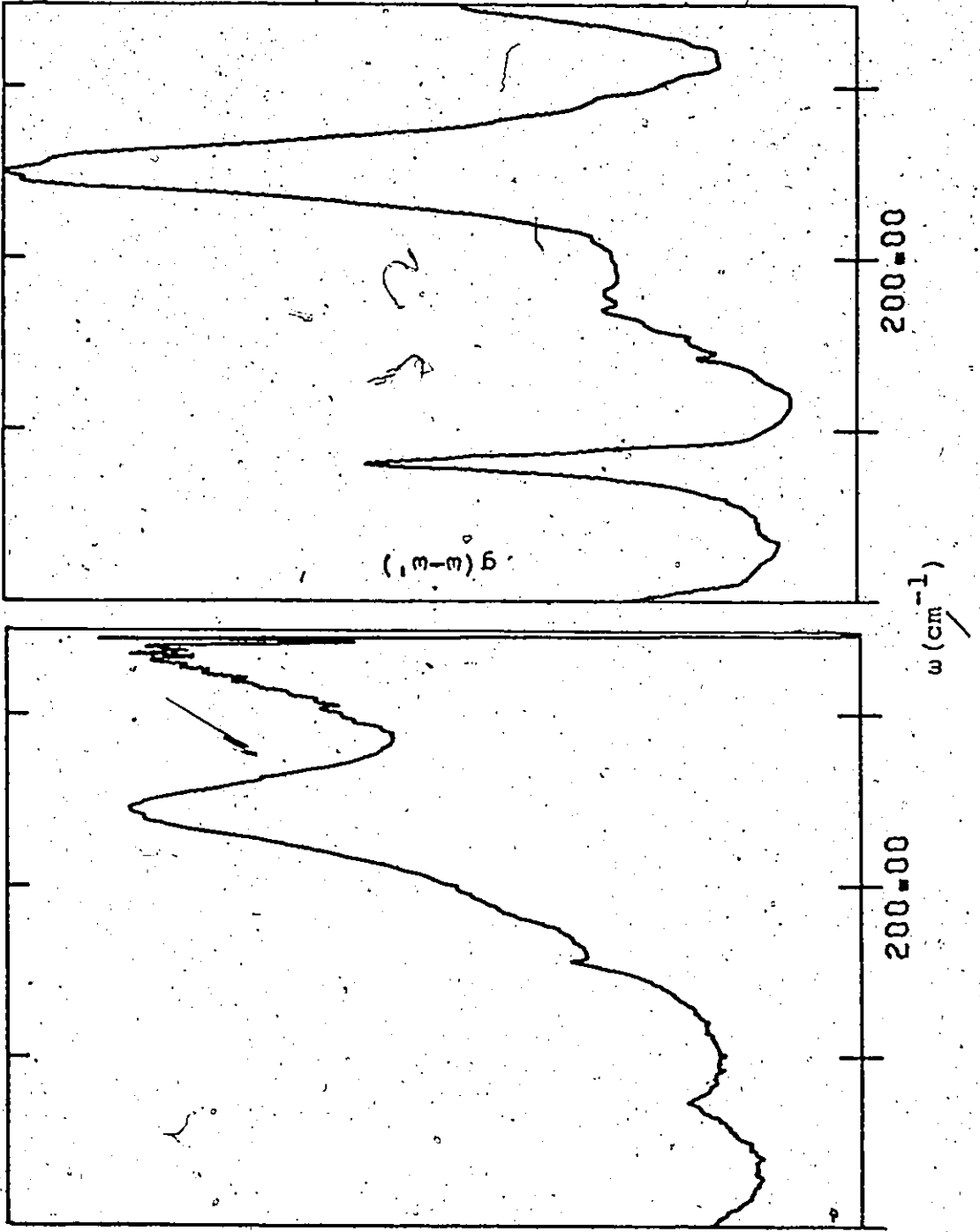
Position (cm^{-1})	Combination	Shape	Critical Pt. Location
459	$\nu_2 + \nu_6$	P_2	Hexagonal Face
490	$\nu_3 + \nu_{4,5}$	$P_1 + P_2$	Hexagonal Face
508	Unknown	-	-
529	$\nu_3 + \nu_6$	$P_1 + P_2$	Hexagonal Face

$2\nu_6$ mode with the help of the experimental dispersion curves. Not only do these assignments look reasonable from the dispersion curves, the actual form of the absorptions lends some credence. To actually define the critical point location and shape attributed to these absorptions is beyond the information given in the density of states and contour plots we have. We believe though that these absorptions could very possibly be due to degenerate P_1 and P_2 (this would account for the shape of the peak at 678 cm^{-1}) type discontinuities on the hexagonal face of the Brillouin zone. This idea will be discussed more fully in Chapter VI.

One final point should be mentioned before continuing to difference mode absorption. It should be noted that the absorption increases almost linearly past 700 cm^{-1} . This is due to the filtering system. Past 700 cm^{-1} very little light intensity is reaching the sample and as we proceed to higher energies more is being cut off. This results in what one might mistakenly consider sample absorption.

Only three (possible) difference mode absorptions were observed in this experiment. The investigation of these difference modes is the most sensitive test of the theoretical calculation and the theory seems to survive the test relatively well. The low frequency region shown in Figure 5.3 with the corresponding density of states consists of features at 149 cm^{-1} , 182 cm^{-1} and 218 cm^{-1} . First let us note that (the sum bands do possess some

Figure 5.3: Observed absorption compared with the calculated density of states for the two-phonon difference processes in the range $120\text{-}260\text{ cm}^{-1}$. The scale is 40 cm^{-1} per inch.



ABSORPTION (ARBITRARY UNITS)

temperature dependence) the $2\nu_{1,2}$ modes at X, that were discussed previously, cause the feature at 182 cm^{-1} . The absorption at 149 cm^{-1} is attributed to the $\nu_6-\nu_3$ mode. The critical point analysis indicates very strong degenerate P_1 and P_2 type discontinuities on the hexagonal face of the Brillouin zone. Although again we are dealing with the ν_6 mode and under even more sensitive conditions, the results of the critical point analysis seem reasonable. The absorption at 218 cm^{-1} is attributed to the $\nu_{4,5}-\nu_1$ modes. Again the critical point analysis indicates very strong degenerate P_1 and P_2 type discontinuities on the hexagonal face for both modes.

A summary of the discussion on two-phonon absorptions given in this chapter will be given in Chapter VI.

CHAPTER VI

CONCLUSIONS

After this detailed analysis of the two-phonon absorption spectrum, it is possible to draw some general conclusions. The overall shapes, positions and intensities of the two-phonon spectrum agree well with the calculated two phonon density of states curve except when the ν_6 mode is present. This means the initial assumption, that the exact nature and frequency dependence of the photon-phonon coupling mechanism that makes possible the absorption has, in general, slight effect on the shape of the multi-phonon absorption bands, is reasonable. It is shown that the most prominent features of the phonon spectrum do not occur at the high symmetry points but originate on the hexagonal face of the Brillouin zone, often near K and W. A summary of all the features in the two-phonon sum and difference absorption spectra are given in Table 6.1. A majority of the features are attributed to the hexagonal face.

When discussing the three absorptions at 595 cm^{-1} , 644 cm^{-1} and 678 cm^{-1} mention was made that we were fairly confident they occurred on the hexagonal face. Assuming that all these absorptions occur at some critical point on the hexagonal face we can take certain sum combinations which are identified

Table 6.1: Summary of all features on the two-phonon sum and difference absorption spectra in this work.

Position (cm^{-1})	Combination	Shape	Critical Pt. Location
149	$\nu_6 - \nu_3$	$P_1 + P_2$	Hexagonal Face
183	$2\nu_{1,2}$	$P_1 + P_2$	X
218	$\nu_{4,5} - \nu_1$	$P_1 + P_2$	Hexagonal Face
222	$\nu_1 + \nu_2$	P_3	W
242	$2\nu_2$	P_2	Hexagonal Face
304	Reststrahl	-	-
380	$2\nu_3$	$P_1 + P_2$	Hexagonal Face
	$\nu_1 + \nu_{4,5}$	Weak	-
409	$\nu_{1,2} + \nu_{4,5}$	$P_1 + P_3$ (or P_2)	X
424	$\nu_1 + \nu_6$	$P_1 + P_2$	Hexagonal Face
	$\nu_2 + \nu_{4,5}$	Weak	-
432	$\nu_{1,2} + \nu_6$	P_1 (?)	X
438	Localized Mode of Unassociated Al Donors		

(continued next page)

Table 6.1 (continued)

Position (cm^{-1})	Combination	Shape	Critical Pt. Location
459	$\nu_2 + \nu_6$	P_2	Hexagonal Face
490	$\nu_3 + \nu_4, 5$	$P_1 + P_2$	Hexagonal Face
508	Unknown	-	-
529	$\nu_3 + \nu_6$	$P_1 + P_2$	Hexagonal Face
595	$2\nu_4, 5$	-	-
644	$\nu_4 + \nu_5$	$P_1 + P_2$ (?)	Hexagonal Face (?)
678	$\nu_4, 5 + \nu_6$	-	-
	$2\nu_6$	-	-

with confidence ($2\nu_2$, $2\nu_3$, $\nu_3 + \nu_{4,5,6}$, $\nu_{4,5} - \nu_1$) and generate all possible sum and difference combinations. The results shown in Table 6.2 are gratifying especially with regard to the absorptions at 595 cm^{-1} , 644 cm^{-1} and 678 cm^{-1} . Similar manipulation at the X and L points give less accurate results. Table 6.3 gives results in the X direction and Table 6.4 for the L direction. Not only is there a fairly wide discrepancy in the experimental and calculated values but modes are degenerate when from the experimental two-phonon absorption curve they do not seem to be.

The lattice vibrations of cubic ZnS have been the subject of a number of investigations in recent years. In all cases any two-phonon combinations have been interpreted using only four critical points, most often $\Gamma(0,0,0)$, $X(1,0,0)$, $L(0.5,0.5,0.5)$ and $W(1,0.5,0)$. This work has tried not to limit interpretation only to the four major critical points. The results of some earlier work are compared with our results in Table 6.5. The shape analysis is not compared since little previous work has been done on it.

Table 6.2: Algebraic generation of sum modes on the hexagonal face of the Brillouin zone using the $v_{4,5}-v_1$, $2v_2$, $2v_3$ and $v_3+v_{4,5,6}$ modes as starting point. A comparison is made to experimental features.

$2v_2 = 242 \text{ cm}^{-1}$	$v_2 = 121$	
$2v_3 = 380 \text{ cm}^{-1}$	$v_3 = 190$	
$*v_3+v_4 = 490 \text{ cm}^{-1}$	$v_4 = 300$	
$*v_3+v_5 = 497 \text{ cm}^{-1}$	$v_5 = 307$	
$v_3+v_6 = 529 \text{ cm}^{-1}$	$v_6 = 339$	
$*v_4-v_1 = 215 \text{ cm}^{-1}$	$v_1 = 85$	} $v_1 = 87$
$*v_5-v_1 = 218 \text{ cm}^{-1}$	$v_1 = 89$	

Experiment

$2v_1 = 174$		
$v_1+v_2 = 208$		
$2v_2 = 242$	242	
$v_1+v_3 = 277$		
$v_2+v_3 = 311$		
$2v_3 = 380$	380	
$v_1+v_4 = 387$		
$v_2+v_4 = 421$		
$v_3+v_4 = 490$	490	
$2v_4 = 600$	595	(590-620)
$v_1+v_5 = 394$		
$v_2+v_5 = 428$		
$v_3+v_5 = 497$	490	

(continued next page)

Table 6.2 (continued).

$\nu_4 + \nu_5 =$	607	595	(590-620)
$2\nu_5 =$	614	595	(590-620)
$\nu_1 + \nu_6 =$	426	424	
$\nu_2 + \nu_6 =$	460	459	
$\nu_3 + \nu_6 =$	529	529	
$\nu_4 + \nu_6 =$	639	644	
$\nu_5 + \nu_6 =$	646	644	
$2\nu_6 =$	678	678	

* $\nu_3 + \nu_{4,5}$ and $\nu_{4,5} - \nu_1$ are not assumed degenerate.

Note: Experimental frequencies in brackets give the width of the absorption; unbracketed frequencies give the frequency corresponding to the maximum point of absorption. All frequencies in Tables 6.2, 6.3 and 6.4 are in cm^{-1} .

Table 6.3: Algebraic generation of sum modes at the X point.

A comparison is made to some experimental features and for peaks at 595 cm^{-1} , 644 cm^{-1} and 678 cm^{-1}

$$2\nu_{1,2} = 183 \text{ cm}^{-1}$$

$$\nu_{1,2} = 91.5$$

$$\nu_{1,2} + \nu_{4,5} = 409 \text{ cm}^{-1}$$

$$\nu_{4,5} = 317.5$$

$$\nu_{1,2} + \nu_6 = 431 \text{ cm}^{-1}$$

$$\nu_6 = 339.5$$

From the dispersion curve $\nu_3 = 216 \text{ cm}^{-1}$ (corrected for liquid helium temperatures)

$$\nu_{1,2} = 92$$

$$\nu_3 = 216$$

$$\nu_{4,5} = 318$$

$$\nu_6 = 340$$

Experiment

$$2\nu_1 = 2\nu_2 = \nu_1 + \nu_2 = 184$$

183

$$\nu_{1,2} + \nu_3 = 308$$

$$2\nu_3 = 432$$

$$\nu_{1,2} + \nu_{4,5} = 410$$

409

$$\nu_3 + \nu_{4,5} = 534$$

$$2\nu_4 = 2\nu_5 = \nu_4 + \nu_5 = 636$$

595

$$\nu_{1,2} + \nu_6 = 432$$

432

$$\nu_3 + \nu_6 = 556$$

$$\nu_{4,5} + \nu_6 = 658$$

644

$$2\nu_6 = 680$$

678

Table 6.4: Algebraic generation of sum modes at the L point. All frequencies are taken from the experimental dispersion curve and corrected to liquid helium temperature. A comparison is made to experimental features at 595 cm^{-1} , 644 cm^{-1} and 678 cm^{-1} .

$$\nu_{1,2} = 71 \text{ cm}^{-1}$$

$$\nu_3 = 199 \text{ cm}^{-1}$$

$$\nu_{4,5} = 295 \text{ cm}^{-1}$$

$$\nu_6 = 344 \text{ cm}^{-1}$$

Experiment

$$2\nu_1 = 2\nu_2 = \nu_1 + \nu_2 = 142$$

$$\nu_{1,2} + \nu_3 = 270$$

$$2\nu_3 = 398$$

$$\nu_{1,2} + \nu_{4,5} = 366$$

$$\nu_3 + \nu_{4,5} = 494$$

$$2\nu_4 = 2\nu_5 = \nu_4 + \nu_5 = 590$$

595

$$\nu_{1,2} + \nu_6 = 415$$

$$\nu_3 + \nu_6 = 543$$

$$\nu_{4,5} + \nu_6 = 639$$

644

$$2\nu_6 = 688$$

678

Table 6.5: Comparison of two-phonon assignments of various workers

Previous Work		This Work	
Position	Assignment	Position	Assignment
Deutsch Nilsen (77°K)	Irwin		
-	-	149	$v_6 - v_3$ Hex. Face
-	176 2TA (X)	183	$2v_{1,2}$ (X)
-	-	218	$v_{4,5} - v_1$ Hex. Face
-	219 $2W_6$	222	$v_1(W) + v_2(W)$
-	-	242	$2v_2$ Hex. Face
-	295 $2W_5, LA(X) + TA(X)$	-	-
-	386 2LA (L)	380	$2v_3$ Hex. Face
-	-	409	$v_{1,2}(X) + v_{4,5}(X)$
431	422 2LA (X)	424	$v_1 + v_6$ Hex. Face
-	-	432	$v_{1,2}(X) + v_6(X)$
455	448 2TA (X) + TO (Γ)	459	$v_2 + v_6$ Hex. Face
491	- 2TA (L) + LO (Γ), $2W_6 + TO$ (Γ)		
-	TO (L) + LA (L)	490	$v_3 + v_{4,5}$ Hex. Face
-	511 TO (X) + LA (X)		

(continued next page)

Table 6.5: (continued)

Position	Previous Work Assignment	Position	This Work Assignment
Deutsch Nilsen (77°K) (R.T.)	Irwin		
526	- 2TA(X)+LO(F), LO(L)+LA(L)	529	$\nu_3 + \nu_6$ Hex. Face
594	- 2TO(L)	595	$2\nu_4, 5, \nu_4 + \nu_5$ Hex. Face
- 612	2TO(X), $2W_2, 2W_3$	644	$\nu_4, 5 + \nu_6$ Hex. Face
- 636	LO(X)+TO(X), LO(L)+TO(L)		
	$2W_1$		
- 665	2LO(X)	678	$2\nu_6$ Hex. Face
667	2LO(X)		

Note: Irwin gives $W_1 = 318$, $W_2 = 306$, $W_3 = 306$, $W_4 = 175$, $W_5 = 147$ and $W_6 = 110$.

All frequencies are in cm^{-1} .

BIBLIOGRAPHY

- Balkanski, M., Nusimovici, M. and Le Toullec, R., 1964, J. Phys. 25, 305.
- Bergsma, J., 1970, Phys. Lett. A 32, 324.
- Birman, J., 1963, Phys. Rev. 131, 1489.
- Banerjee, R. and Varshni, Y.P., 1969, Can. J. Phys. 47, 451.
- Borik, H., 1970, Phys. Stat. Sol. 39, 145.
- Brafman, O. and Mitra, S.S., 1968, Phys. Rev. 171, 931.
- Cano, R. and Mattioli, M., 1967, Infrared Phys. 7, 25.
- Connes, J. and Connes, P., 1966, J. Opt. Soc. Amer. 56, 896.
- Cooley, J.W. and Tukey, J.W., 1965, Mathematics of Computation 19, 296.
- Cowley, E. R. and Cowley, R. A., 1965, Proc. Roy. Soc. A287, 259.
- Deutsch, T., 1962, Proc. Int. Conf. Phys. Semicond., Exter, (The Institute of Physics and the Royal Society, London), p. 505.
- Dolling, G., 1974, private communication.
- Dolling, G. and Waugh, J.L., 1965, Lattice Dynamics ed. by R. F. Wallis (Pergamon), Oxford, p. 19.
- Douglas, R.J. and Timusk, J., 1974, Appl. Opt. 13, 723.
- Feldkamp, L.A., Steinman, D.K., Vagelatos, N. and King, J.S., 1971, J. Phys. Chem. Solids 32, 1573.
- Feldkamp, L.A., Venkataraman, G. and King, J.S., 1969, Solid State Commun. 7, 1571.
- Fellgett, P.R., 1951, Thesis, University of Cambridge.

- Forman, M.J., Steel, W.H. and Vanasse, G.A., 1966, J. Opt. Soc. Amer. 56, 59.
- Geick, R., 1965, Phys. Rev. 138, A1495.
- Ibuki, S., Komiya, H., Mitsuishi, A., Manabe, A. and Yoshinaga, H., 1968, International Conference on Semiconductors, Moscow, p.1047
- Irwin, J.C., 1970, Can. J. Phys. 48, 2477.
- Jacquinet, P. and Dufour, C., 1948, J. Rech. du Centre Mat. Rech. Sci. Lab., Bellevue (Paris) 6, 91.
- Johnson, F.A., 1965, Progr. Semicond. 9, 179.
- Kleinman, D., 1960, Phys. Rev. 118, 118.
- Koteles, E.S., 1973, Thesis, McMaster University.
- Loewenstein, E., 1966, Appl. Opt. 5, 845.
- Marshall, R. and Mitra, S.S., 1964, Phys. Rev. 134, 1019.
- Nilsen, W.G., 1969, Phys. Rev. 182, 838.
- Phillips, J. C., 1956, Phys. Rev. 104, 1263.
- Tumber, A., 1968, M.Sc. Thesis, McMaster University.
- Vagelatos, N., Wehe, D. and King, J.S., 1974, J.Chem. Phys. 60, 3613.
- Yarnell, J.L., Warren, J.L., Wenzel, R.G. and Dean, P.J., 1968, Neutron Inelastic Scattering, Vol. 1, Vienna, p. 301.
- Ziman, J.M., 1972, Principles of the Theory of Solids (Cambridge University Press), Cambridge, p. 271.
- Zwerdling, S., Smith, R.A. and Theriault, J.P., 1968, Infrared Phys. 8, 271.
- Zwerdling, S., Theriault, J.P. and Reichard, H.S., 1968, Infrared Phys. 8, 135.